Developments in the Built Environment 16 (2023) 100275

Contents lists available at ScienceDirect

Developments in the Built Environment

journal homepage: www.sciencedirect.com/journal/developments-in-the-built-environment

# Monitoring early age elastic and viscoelastic properties of alkali-activated slag mortar by means of repeated minute-long loadings

Ali Naqi [a,*], Brice Delsaute [a], Markus Königsberger [a,b], Stéphanie Staquet [a]

[a] BATir Department, Université Libre de Bruxelles, CP194/02, 50 Avenue F.D. Roosevelt, Brussels 1050, Belgium
[b] Institute for Mechanics of Materials and Structures, TU Wien, Karlsplatz 13/202, Vienna 1040, Austria

ARTICLE INFO

*Keywords:*
Alkali-activated materials
Heat release compressive strength
Elastic stiffness
Creep

ABSTRACT

This study investigates the development of elastic and creep properties of sodium hydroxide-activated blast furnace slag mortar, utilizing three different molarities of the activator solution and two solution-to-binder ratio and a reference OPC-based mixture, since the earliest age. The experimental phase involves a series of hourly-repeated 5-min long creep tests on the aging material. This approach enables continuous monitoring, facilitating the characterization of early-age elastic stiffness and creep properties. Linear regression is employed to calculate the tangent unloading (elastic) modulus and Poisson's ratio. To model short-term creep behaviour, a power-law creep function is utilized. The integration of these findings with calorimetry-derived evolutions of cumulative heat release establishes linear correlation between (compressive) strength and heat release, along with a power function relationship between unloading (elastic) modulus and heat release. An optimal alkali dosage ($Na_2O$ content) appears to be vital for long-term strength development. Additionally, the creep parameters, namely amplitude (A) and kinetic (K), demonstrate a gradual decrease, although they maintain values higher than those of the corresponding OPC mixture, as the heat release progresses.

## 1. Introduction

Growing environmental concerns attributed to high carbon emissions from Portland cement production have prompted researchers to seek alternatives that mitigate carbon footprints and address global warming (Lothenbach et al., 2011; Bijen, 1996; Li et al., 2021; Dai et al., 2022; Naqi et al., 2023). Industrial by-products like ground granulated blast furnace slag (GGBFS) and fly ash (FA), when activated with alkaline components such as sodium hydroxide and water glass, have demonstrated not only promising but even superior mechanical properties compared to Portland cement (Hardjito et al., 2004; Juenger et al., 2011; Provis et al., 2015). Several studies have explored the utilization of GGBFS as a sole binder to enhance the overall sustainability of concrete production (Bijen, 1996; Bakharev et al., 2003; Wang and Scrivener, 1995; Roy, 1999).

In practical civil engineering, the durability of concrete structures is closely connected to both chemical processes and mechanical properties during the early stages. The rapid changes in characteristics like hydration, stiffness, creep, strength, and shrinkage significantly influences the serviceability, durability, and, most importantly, the safety of structures (Serdar et al., 2020). Understanding the potential for concrete cracking demands a clear grasp of its viscoelastic behaviour, particularly in the early stages (Delsaute et al., 2017). Concrete creep has been a topic of study for more than a century (Brooks, 2005; Bažant and Xiang, 1997). Over the years, numerous predictive models have been proposed to estimate long-term deformations, which serve as essential references for the structural design of concrete structures. Various theories have been proposed to gain a deeper understanding of creep behaviour in concrete structures, including the seepage theory (Powers, 1968), the interlayer theory (Feldman, 1968), the viscous shear theory (Walter, 1968), the thermal activation theory (Wittmann, 1973) and Bažant's et al. (Bažant et al., 1997) microprestress-solidification theory; that appears to be an extension to author's previous solidification theory. A comprehensive overview of the creep mechanisms of C–S–H (calcium--silicate-hydrate) can be found in the literature (Tamtsia and Beaudoin, 2000; Ye, 2015).

It is widely accepted that creep and relaxation result from the viscoelastic behaviour of the reaction products (Neville, 1964; Bažant and Prasannan, 1988). Previous research, highlighted by Brooks (2005), Bazant (Bažant and Xiang, 1997), and Li (Bažant and Li, 2008), involved classical creep tests on concrete that can last from days to years. These longer tests can be affected by factors like changing humidity and

* Corresponding author.
*E-mail address:* Ali.Naqi@ulb.be (A. Naqi).

https://doi.org/10.1016/j.dibe.2023.100275
Received 30 August 2023; Received in revised form 19 October 2023; Accepted 12 November 2023
Available online 18 November 2023

temperature over time, making their interpretation complex. Furthermore, the coupling between the continuously evolving hydration products and the simultaneous development in material properties (Irfan-Ul-Hassan et al., 2016), all while samples are under load, further complicates the study of time-dependent deformations. Consequently, accurately predicting the contribution of each factor in creep theories poses a significant challenge.

The predictive models developed in the past to monitor the evolution of concrete properties were constructed upon extensive experimental datasets. However, they primarily focused on hardened concrete, lacking the capability to forecast the viscoelastic behaviors in its very early stages of hardening (Delsaute et al., 2016a, 2017). Given this limitation, the significance of monitoring the developments of both elastic (Young's modulus) and viscoelastic properties (basic creep) from the very early stages of concrete production becomes even more apparent, especially for emerging concrete formulations, where traditional models may not provide accurate predictions (Serdar et al., 2020).

To address the aforementioned problem in measuring (aging) creep, Irfan-ul-Hassan et al. (Irfan-Ul-Hassan et al., 2016) and Delsaute et al. (2017) introduced a novel experimental methodology. Their approach involves conducting compressive creep tests on fresh paste/mortar mixtures, with hourly repetitions, during the initial days of hydration, starting from the moment of final setting. These tests were performed with loading periods of 3 and 5-min, respectively. Furthermore, the applied loading was 15 % and 20 %, respectively, ensuring that the samples remained undamaged and operated within the linear creep range (Ruiz et al., 2007). During these brief loading intervals, the microstructure of the sample remains virtually constant, indicating non-aging creep. However, the microstructure undergoes changes between successive tests, resulting in intrinsic aging and a continuous evolution of creep properties over time. In each short-term creep test, creep behaviour is characterized using either a power-law (Irfan-Ul-Hassan et al., 2016; Göbel et al., 2018a) or logarithmic law-type creep function (Delsaute et al., 2017). These short-term creep testing protocols have proven to be highly effective, not only when applied to cement-based binders at paste (Irfan-Ul-Hassan et al., 2016), mortar (Irfan-ul-Hassan et al., 2017), and concrete scales (Delsaute et al., 2017; Ausweger et al., 2019), but also to the blend cements (Göbel et al., 2018a; Schmid et al., 2023). Although, considerable research has investigated the early-stage creep behaviour in cement-based systems through different techniques (Vandamme and Ulm, 2013; Jones and Grasley, 2011; Chen et al., 2017; Wyrzykowski et al., 2019; Hu et al., 2020; Hu et al., 2021), there has been no research conducted on the early-age creep properties of alkali-activated systems.

This study aims to fill this gap by investigating whether short-term creep testing methods can be used effectively for alkali-activated systems. The hydration process of GGBFS varies significantly from traditional OPC systems. Hence, this study undertakes the challenging task of effectively defining the early-age creep behaviour and precisely predicting the (aging) viscoelastic deformation in slag-based mixtures with varying molarities. Additionally, a range of load rates spanning from 5 s to 300 s and different load magnitudes ranging from 5 % to 40 % of compressive strength are employed to analyse the effects of loading rate and loading magnitude on the viscoelastic deformations of slag mortar samples.

## 2. Experimental program

### 2.1. Raw materials

CEM I 52.5 N type ordinary Portland cement (OPC) and ground granulated blast furnace slag (GGBFS) were utilized as binders in this study. Detailed oxide compositions of both binders are provided in Table 1. The density of OPC was 3.15 g/cm$^3$, while GGBFS exhibited a density of 2.92 g/cm$^3$. For the activation of GGBFS, a powdered form of sodium hydroxide (NaOH), commonly referred to as caustic soda, with a purity of 97 %, was utilized as the activator.

### 2.2. Mix compositions and mixing procedure

The details of the mortar mixes utilized in this study were presented in Table 2. An alkaline activator was prepared using sodium hydroxide (NaOH) as the alkaline compound. Sodium hydroxide anhydrous pearls were mixed with distilled water to create different molarity concentrations: 0.5, 2 and 8 M. The molarity increased by a factor of 4 for each activation attempt. The alkaline solutions were prepared 24 h prior to mixture preparation. For the mortar samples, oven-dried silicious sand (0/4 mm) was used as fine aggregate. Two groups of alkali-activated mortar (AAM) mixtures and one OPC-based reference mixture was prepared to investigate the impact of different molarity concentrations and solution or water-to-binder (S or W/B) ratios on the early age elastic and viscous properties. It is noteworthy that in case of AAM mixtures, the S/B ratio remained constant for each group of molarity concentration, resulting in varying water-to-binder ratios (W/B) due to the presence of alkalis in the systems.

In the first group, the S/B ratio remained constant at 0.5 for three molarity concentrations. Consequently, the corresponding water-to-binder (W/B) content and sodium oxide ($Na_2O$) content varied from 0.37 to 0.49 and from 9.76 % to 0.76 %, respectively. In the second group, the S/B ratio was fixed at 0.8 for three molarity concentrations, resulting in corresponding W/B content and $Na_2O$ content ranging from 0.60 to 0.78 and from 15.61 % to 1.22 %, respectively. The sand-to-paste ratio was set at 1 for all studied samples. This selection led to a corresponding sand-to-slag (binder) ratio of 1.5 for the first set of mixtures, prepared with an S/B ratio of 0.5. Meanwhile, the second set of mixtures, prepared with an S/B ratio of 0.8, resulted in a sand-to-slag ratio of 1.8. The most concentrated mixture, denoted as 8 M and prepared with an S/B ratio of 0.5 and W/B ratio of 0.37, was chosen as the benchmark composition. Preliminary tests on this mixture revealed that a sand-to-paste ratio exceeding 1 significantly compromised the homogeneity of the mixture. This means that the mixer was unable to blend a high quantity of sand in such a high concentration mixture, ultimately resulting in a non-homogenous and unworkable blend. Therefore, to maintain consistency across all remaining mixtures, a sand-to-paste ratio of 1 was adopted. It is important to note that the water content absorbed by the sand, with a coefficient of absorption of 1.99 %, was not considered in these mixture proportions. As a result, the effective W/B ratio for all studied compositions remained consistently lower than the values presented in Table 2. The designation "REF" indicated the OPC-based reference composition, while the AAM mixtures were labelled with their respective molarity concentration, followed by the S/B ratio. For instance, the first mix was labelled as 8 M – 0.5SB, signifying a molarity of 8 M and an S/B ratio of 0.5.

Fresh mortar mixtures were prepared using a 20-L capacity mixer in the following manner: the activator solution was poured into the mixing

**Table 1**
Oxide composition of OPC and GGBFS (Carette and Staquet, 2016; Dai et al., 2020).

| Binders | CaO | $SiO_2$ | $Al_2O_3$ | MgO | $SO_3$ | $TiO_2$ | $K_2O$ | $Na_2O$ | $Fe_2O_3$ | MnO |
|---|---|---|---|---|---|---|---|---|---|---|
| OPC (%) | 60.39 | 21.37 | 5.69 | 2.41 | 3.10 | 0.47 | 0.67 | 0.28 | 3.06 | 0.09 |
| GGBFS (%) | 40.80 | 33.30 | 12.30 | 7.84 | 2.30 | 1.29 | 0.67 | 0.44 | 0.39 | 0.36 |

**Table 2**
Mixture design for OPC and GGBFS mortar mixtures (kg/m3).

| Series | Mix ID | NaOH (mol/L) | Binder (kg) | Sol. (kg) | Water (kg) | Sand (kg) | S/B | W/B | $Na_2O$[a] (%) |
|---|---|---|---|---|---|---|---|---|---|
| REF | OPC – 0.5WB | – | 708 | – | 354 | 1062 | – | 0.50 | – |
| AAM | 8 M – 0.5SB | 8 | 750 | 375 | 281 | 1125 | 0.5 | 0.37 | 9.76 |
| S/B | 2 M – 0.5SB | 2 | 710 | 355 | 329 | 1065 | 0.5 | 0.46 | 2.88 |
| ratio = 0.5 | 0.5 M – 0.5SB | 0.5 | 700 | 350 | 343 | 1050 | 0.5 | 0.49 | 0.76 |
| AAM | 8 M – 0.8SB | 8 | 595 | 476 | 357 | 1071 | 0.8 | 0.60 | 15.61 |
| S/B | 2 M – 0.8SB | 2 | 554 | 443 | 410 | 997 | 0.8 | 0.74 | 4.61 |
| ratio = 0.8 | 0.5 M – 0.8SB | 0.5 | 545 | 436 | 427 | 981 | 0.8 | 0.78 | 1.22 |

[a] Mass percentage of GGBFS.

bowl, followed by the addition of the precursor (GGBFS). Mixing was performed at a low speed of 300 ± 10 rpm for 60 s, and then the mixing speed was increased to high speed (500 ± 10 rpm) for an additional 30 s. Subsequently, the sand was added to the paste mixture within 30 s while the mixer was still at low speed, and then the mixing speed was switched to high speed for an additional 30 s. The mixer was then rested for 90 s, the bowl was scraped, and the mixing process concluded with 60 s of high-speed mixing.

### 2.3. Experimental techniques

#### 2.3.1. Isothermal calorimetry

The heat flow from the paste mixture was recorded using an eight-channel TAM Air isothermal conduction calorimeter at 20 °C for a duration of 7 days after mixing. This allowed for the measurement of both the direct heat flow and the cumulative heat release Q(t). Paste samples were prepared externally and immediately filled into glass vials. The vials were then sealed and loaded into the calorimeter for testing. To ensure accurate measurements, the initial 1-h data was excluded from the cumulative heat release data. This exclusion was necessary because the sample preparation time took approximately 15 min, and an additional 45 min was required for the calorimeter to reach thermal stability due to the thermal disturbance caused by the insertion of the sample (Hu et al., 2014). However, it is suggested that the total heat released during this initial period is relatively insignificant compared to the total heat release by the paste, as also documented in the literature (Lenormand et al., 2015).

#### 2.3.2. Compressive strength

The compressive strength of slag mortar samples was determined on 50 mm cubes that were cured in sealed condition. After casting, the samples were stored in a temperature-controlled chamber at 20 °C. Demoulding was conducted after 24 h, and the samples were then wrapped in plastic sheets and placed back in the climatic chamber until testing. For each testing age, an average of three samples was taken to obtain the strength value.

#### 2.3.3. Short-term creep testing

*2.3.3.1. Test setup.* Uniaxial compressive creep measurements were conducted on cylindrical samples with a diameter of 97 mm and a height of 550 mm. In order to monitor the free strains (thermal and autogenous), a companion cylindrical sample, referred to as a dummy sample, was also prepared with the same dimensions as the loaded specimen. After casting, the mortar mixture was poured into a Polyvinyl chloride (PVC) mould and stored in a temperature-controlled chamber at 20 °C The samples were demoulded a few hours after the final setting and then ground on both faces to ensure flat surfaces. Subsequently, they were wrapped in two self-adhesive aluminium sheets to maintain full sealing and prevent drying.

The creep test was conducted using a Walter + Bai LFMZ 100 kN electromechanical testing machine, which was located in a climatic room maintained at a constant temperature of 20 °C. An Invar© extensometer, consisting of two rings, was attached to the sample using three anchorages with elastic blades per ring (refer to Fig. 1). The initial length, also referred to as the base length or measurement length, between the two rings was set to 350 mm. To ensure accurate measurements, the length changes were recorded in the central part of the sample, which is a zone practically free of shear stresses. This was done to eliminate any edge effects resulting from friction at the interface between the sample and the load platens (Karte et al., 2015). or displacement measurement, three longitudinal displacement sensors were placed at 120° intervals around the specimen. These sensors had a maximum stroke of 0.5 mm and were used to measure the displacement between the two rings. Additionally, three transversal displacement sensors, also placed at 120° intervals around the sample, measured the transversal length change between the lower ring and the sample.

*2.3.3.2. Test protocol.* The short-term creep testing protocol involved subjecting the sample to hourly-repeated minute-long compressive loadings. Fig. 2 illustrates a schematic diagram of one cycle of the short-term creep test. The load applied during each test was set at 20 % of the sample's compressive strength at the time of testing. The loading was force-controlled and applied within 10 s, maintaining a constant force. Once the desired stress level was reached, the load was kept constant for 5 min (300 s). Subsequently, the load was removed within 10 s. It is important to note that at this load level, the samples remained undamaged and remained within the elastic range (Ruiz et al., 2007). To validate this assumption, the dummy specimen was loaded for a few cycles at the end of the test. This validation process demonstrated that the creep strains induced during the short-term creep test, which consisted of a 300-s force plateau, were fully recoverable., see Fig. 18 of Ref (Irfan-Ul-Hassan et al., 2016). To ensure proper contact between the load cell and the specimen, a constant compressive load of 0.3 kN was applied to the sample during the 1-h recovery time between two consecutive creep tests. Since the recovery time between tests was significantly longer than the duration of the creep test itself, subsequent

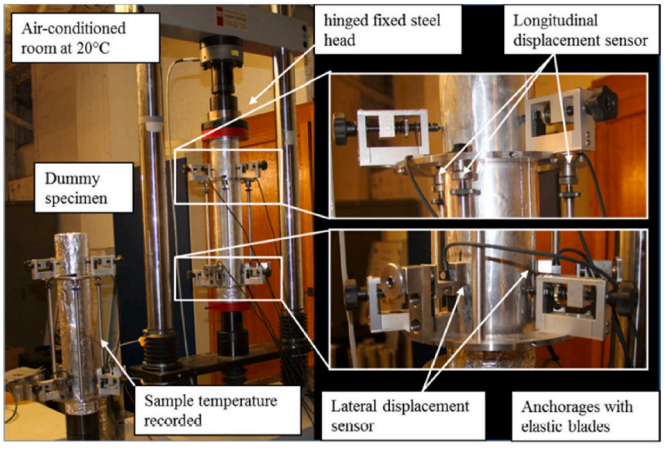


**Fig. 1.** Test setup consisting of mortar cylindrical loaded and dummy sample, two Invar rings holding longitudinal and lateral displacement sensors (spacing 120°) around the sample (Delsaute and Staquet, 2019).

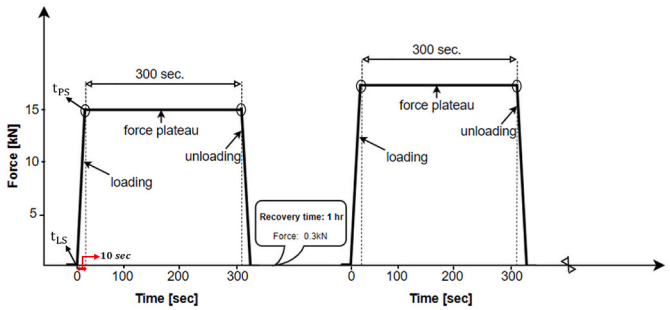


**Fig. 2.** Scheme of two successive repeated creep tests in the context of 5-min long creep test.

creep test cycles were conducted on the same sample starting from a fully recovered configuration. Furthermore, a strategy was developed to enable the continuous monitoring of multiple mixes in the test setup. Initially, hourly-repeated minute-long loadings were performed during the early stages when the hardening process is most active. Subsequently, tests were conducted at specific ages, such as 28, 90 and 180 days, to assess the long-term evolution of viscoelastic properties. This approach allowed for the simultaneous testing of multiple mixtures during the same period.

*2.3.3.3. Test evaluation.* The evolution of uniaxial stress $\sigma(t)$ is defined as

$$\sigma(t) = \frac{F(t)}{A} \tag{1}$$

where $F(t)$ is the applied compressive force, as a function of time, and A is the cross-sectional area of the tested sample, $A = 7390mm^2$.

From each 5-min creep test, the total strain evolutions were measured based on the longitudinal displacement sensor readings as follows:

$$\varepsilon_{tot}^{exp}(t) = \frac{1}{350mm}\sum_{i=1}^{3}\frac{\Delta\ell_i(t)}{3} \tag{2}$$

where $\Delta\ell_i$ represents three longitudinal sensor readings, averaged, and divided by the measurement length (350 mm) to quantify the total longitudinal strain evolution.

The elastic modulus was estimated by performing linear regression on the stress and strain measurements obtained during loading and unloading events, specifically between 20 % and 80 % of the load range (Delsaute et al., 2016b). Both the loading and unloading modulus yielded the same estimate of the elastic modulus. However, in this study, only the unloading modulus was considered for a specific creep test. The instantaneous elastic strains, $\varepsilon_{el}(t)$, can be quantified from the uniaxial stress, $\sigma(t)$, and the unloading (elastic) modulus, $E_{un}$. Creep strains, $\varepsilon_{cr}(t)$, can be derived by subtracting the total measured longitudinal strains, $\varepsilon_{tot}(t)$, and free strains, $\varepsilon_{fr}(t)$, and the instantaneous elastic strains, $\varepsilon_{el}(t)$:.

$$\varepsilon_{cr}(t) = \varepsilon_{tot}(t) - \varepsilon_{fr}(t) - \varepsilon_{el}(t) = \varepsilon_{tot}(t) - \frac{\sigma(t)}{E_{un}} \tag{3}$$

The basic creep behaviour, of short-term creep test, is described in terms of a compliance function $''J'$ (units in $MPa^{-1}$), or as a ratio of elastic deformation, known as creep coefficient $''\varphi_c''$. Compliance is a unit of strain per stress as shown in (4).

$$J(t,t') = \frac{\varepsilon_{tot}(t,t')}{\sigma(t')} = \frac{\varepsilon_{el}(t') + \varepsilon_{cr}(t,t')}{\sigma(t')} = \frac{1}{E_{un}} + C(t,t') \tag{4}$$

where $J(t,t')$ is the compliance as a function of time (t), and loading age $(t')$, $\varepsilon_{tot}$ is the total strain in the loaded specimen in m/m, σ is the stress applied in MPa, $\varepsilon_{el}$ is the elastic strain in m/m, $\varepsilon_{cr}$ is the creep strain in m/m. $E_{un}$ is the unloading (elastic) modulus in MPa, and C is the specific creep in $MPa^{-1}$. The basic creep coefficient $''\varphi_c''$ for which the link with the unloading (elastic) modulus and the creep compliance is given in (5).

$$J(t,t') = \frac{1+\varphi_c(t,t')}{E_{un}}, \because \varphi_c(t,t') = \frac{\varepsilon_{cr}(t,t')}{\varepsilon_{el}(t')} \tag{5}$$

Where $\varphi_c(t,t')$ is the creep coefficient, ratio between creep strain and elastic strain.

Evaluation of creep experiment was carried out in the context of linear theory of viscoelasticity (Reiss, 1961), considering that loading phase contains both the elastic and time-dependent creep deformations (Irfan-Ul-Hassan et al., 2016; Ausweger et al., 2019; Binder et al., 2023). Boltzmann's superposition principle was used to compute the strain evolution $\varepsilon_{tot}(t)$ in terms of time convolution integral (Boltzmann, 1878).

$$\varepsilon_{tot}(t) = \int_0^t J(t-t')\frac{\partial\sigma}{\partial t}dt' \tag{6}$$

where $J(t-t')$ represents the uniaxial creep function, $\frac{\partial\sigma}{\partial t}$ stands for time-derivative of the stress history. As regard the creep function, a power-law type creep function, first introduced in (Delsaute et al., 2012) was used that utilizes only two fitting parameters, amplitude parameter 'A': linked to the amplitude of creep coefficient after 5-min of loading, and kinetic parameter 'K': linked to the kinetic evolution of the creep coefficient, and reads

$$J(t-t') = \frac{1}{E_{un}} + \frac{A}{E_{un}}\left(\frac{t-t'}{t_A}\right)^K \tag{7}$$

where $t_A = 300s$ is the reference time.

The stress was applied within 10 s during the loading phase, in the time interval $t_{LS} \le t \le t_{PS}$. During the subsequent 300 s (5-min) of stress plateau phase, in the time interval $t > t_{PS}$, the stress vanishes as shown in Fig. 2. Dividing the stress history in number of small steps and inserting eq. (7) into eq. (6) yields following total strains $\varepsilon_{tot}(t)$.

$$\varepsilon_{tot}(t) = \frac{\Delta\sigma}{E_{un}} + \frac{A\left(\frac{\partial\sigma}{\partial t}\right)}{E_{un}}\left(\frac{t_A}{K+1}\right)\left[\left(\frac{t-t_{LS}}{t_A}\right)^{K+1} - \left(\frac{t-t_{PS}}{t_A}\right)^{K+1}\right] \tag{8}$$

where $\Delta\sigma$ denotes the stress increase applied during the loading phase, $t_{LS}$ is the time for start of loading, and $t_{PS}$ is time for start of plateau.

Creep parameters, amplitude 'A' and kinetic 'K,' were identified for each creep test by minimizing the square root of sum of squared errors between the experimentally and modelled obtained total strain evolutions as follows:

$$\varepsilon_{error} = \sqrt{\frac{1}{N}\sum_{i=1}^{N}\left[\varepsilon_{exp}(t_i) - \varepsilon_{mod}(t_i)\right]^2} \tag{9}$$

where 'N' is the number of experimental readings used for the test evaluation, that contain both the loading and holding phase.

The test setup, as shown in Fig. 1, also enabled us to monitor the evolutions of Poisson's ratios from the set of recordings (longitudinal and transversal strains) of whole loading, unloading events and defined as

$$\nu_{el} = \frac{\varepsilon_{el}^{tr}}{\varepsilon_{el}^{la}} \tag{10}$$

where $\varepsilon_{el}^{tr}$, and $\varepsilon_{el}^{la}$ represents transversal and longitudinal strains, respectively.

## 3. Individual test results

### 3.1. Isothermal calorimetry

The normalized heat flow and accumulated normalized heat of the OPC and sodium hydroxide activated pastes, with varying molarity (NaOH concentration) and S/B ratios, up to 7 days, are presented in Fig. 3 (a) and (b), respectively. The first peak in the heat flow curves is linked to the wetting and fast dissolution of small slag grains upon contact with the alkaline activator (Shi and Day, 1995). However, due to thermal disturbance caused by the insertion of the sample, the data corresponding to this peak had to be excluded from the analysis. The heat flow curves presented in Fig. 3 (a) depict the calorimetric evolution after the initial peak. The second exothermic peak observed in the curves corresponds to the formation of primary reaction products (Shi and Day, 1995). Samples with higher molarity concentrations, such as 8 M, exhibited an increase in slope during the accelerating period. Additionally, the main peak in the heat flow curves was found to be higher for mixes with higher molarity concentrations. This can be attributed to the higher alkali content present in these mixes, which promotes a faster and more extensive dissolution of slag and the subsequent formation of reaction products (Shi and Day, 1995; Huanhai et al., 1993). However, the mixture with the lowest molarity concentration, 0.5 M, did not exhibit a noticeable main peak. Furthermore, the reaction acceleration was lower and more prolonged for mixtures with decreasing molarities (from 8 M to 0.5 M) and a lower S/B ratio. The reaction rates are significantly influenced not only by the molarity concentration of the mixtures but also by the S/B ratios and, consequently, the corresponding W/B ratios. For instance, 8 M mixtures with S/B ratios of 0.5 and 0.8 exhibit W/B contents of 0.37 and 0.60, respectively. In isothermal calorimetry, where the samples are fully sealed with no external curing, self-desiccation occurs due to the chemical shrinkage accompanying the slag hydration reactions. This phenomenon results in decreased ongoing reaction rates, with a more pronounced effect in lower W/B pastes (Bentz et al., 2009). Therefore, the 8M-0.5SB mixture, which has a lower W/B content of 0.37, exhibited a lower reaction peak compared to its counterpart, the 8M-0.8SB mixture, which has a higher W/B content of 0.60. A similar trend was observed for the remaining mixtures. The reference OPC mixture showed longer induction period and an intermediate magnitude of the main peak in the heat flow compared to the 8 M and 2 M slag mixtures. However, the cumulative heat release, in case of OPC mixture, is highest compared to all other slag-based mixtures, see Fig. 3 (b). It is noteworthy that, slag-based mixtures with the same S/B ratio and varying W/B content, both the initial rates of the reaction and the maximum heat release were influenced by the concentration of NaOH in the solution. This resulted in higher degrees of reaction with increasing NaOH concentration, as depicted in Fig. 3 (b). This trend is different from what has been observed in cement-based systems, where the initial rates of reaction are barely distinguishable for varying W/B ratios (Bentz et al., 2009; Pang, 2015).

To evaluate and describe the relationship between test results at later ages (7 days onwards), two extrapolation models were employed. The first method involved plotting the cumulative heat Q as a function of the inverse square root of age (ISR), considering that Q linearly increases with decreasing the inverse square root of time. A detailed description of the extrapolation procedure can be found in referenced works (Naqi et al., 2023; Lenormand et al., 2015; Aboulayt et al., 2020; Lacante et al., 2022). The second method utilized an exponential model, originally proposed by Freisleben-Hansen and Pedersen (FHP), which was fitted to the calorimetry curves (Pane and Hansen, 2005; Neithalath, 2008). Eq. (11) represents the exponential function used.

$$Q(t) = Q_{max} \exp\left(-\left[\frac{\tau}{t}\right]^{\beta}\right) \tag{11}$$

where Q(t) represents the obtained total heat at time (t), and $Q_{max}$ is the maximum heat release. The term $\tau$ represents the reaction time parameter that controls the time shift in reaction curve, while β is the reaction slope parameter that shapes the reaction curve (Neithalath, 2008). To adjust the multi-curvature calorimetry evolutions, the above equation was adapted as:

$$Q(t) = a_1 \exp\left(-\left[\frac{\tau_1}{t}\right]^{\beta_1}\right) + a_2 \exp\left(-\left[\frac{\tau_2}{t}\right]^{\beta_2}\right) \tag{12}$$

$$Q_{max} = a_1 + a_2 \tag{13}$$

Fig. 4 depicts the extrapolation procedures and the representative fit to the experimentally obtained calorimetric results of the mixtures with a S/B ratio of 0.5. The solid lines represent the experimentally obtained cumulative heat data up to 7 days, while the dashed lines illustrate the fitted models for later ages. The maximum heat release $Q_{max}$ and other model parameters for all alkali-activated paste samples and OPC mixture listed in Table 3. A comparison of the maximum heat release provided by the two methods revealed that the exponential method (FHP) predicted a lower value of heat release compared to the inverse square root of age function (ISA) for all the studied mixes. It is important to mention that ultimate heat release obtained using exponential function are strongly dependent on the reaction time parameter $\tau$ and reaction slope parameter β. The earlier the reaction time parameter, the more rapid will be the reaction. Furthermore, an increase in reaction slope parameter refers to a faster reaction process. In this study, when referring to the cumulative heat release, the estimation from the inverse square root of age function (ISA) was used. It should be noted that these estimations of $Q_{max}$ based on extrapolation models involved significant uncertainty, as the curve fitting was not well-constrained for high cumulative heat release,

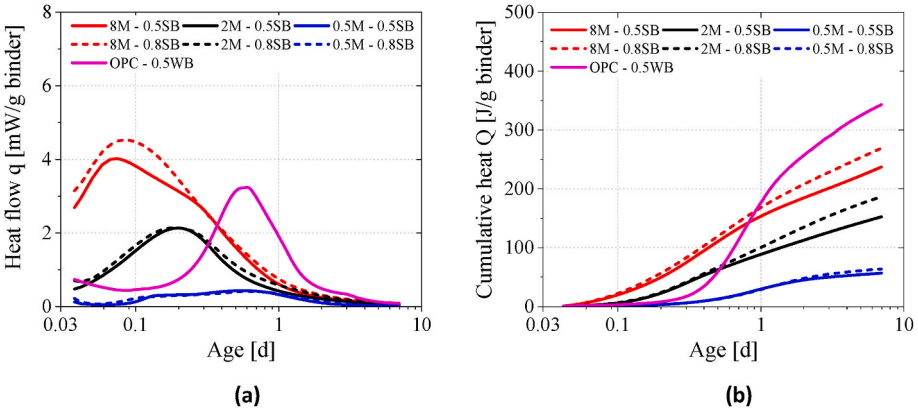


**Fig. 3.** Isothermal calorimetry results of the samples: **(a)** heat flow curves, and **(b)** are the cumulative heat as a function of sample age. All values are normalized per gram of binder (slag/cement).

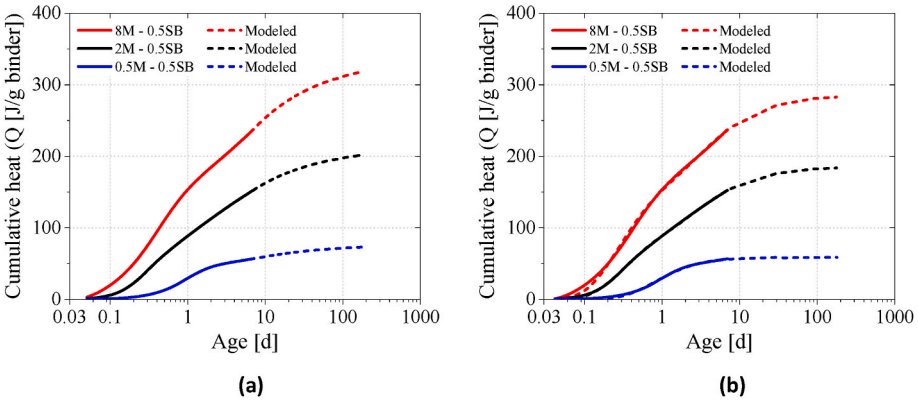


**Fig. 4.** Cumulative heat response of paste samples using **(a)** inverse square root of age function, and **(b)** exponential function.

**Table 3**
Exponential model parameters, and models predicted ultimate heat release $Q_{max}$, of all paste mixes.

| Mix ID | $a_1$ | $\tau_1$ | $\beta_1$ | $a_2$ | $\tau_2$ | $\beta_2$ | $Q_{max}$ (FHP) | $Q_{max}$ (ISR) |
|---|---|---|---|---|---|---|---|---|
| | (J/g) | (d) | (−) | (J/g) | (d) | (−) | (J/g) | (J/g) |
| 8 M – 0.5SB | 201 | 0.5 | 0.6 | 84 | 2.4 | 1.9 | 285 | 338 |
| 2 M – 0.5SB | 123 | 0.7 | 0.5 | 63 | 2.9 | 1.4 | 186 | 214 |
| 0.5 M – 0.5SB | 49 | 2.7 | 0.3 | 14 | 5.2 | 0.2 | 63 | 77 |
| 8 M – 0.8SB | 219 | 1.9 | 0.2 | 110 | 7.0 | 0.6 | 329 | 380 |
| 2 M – 0.8SB | 139 | 2.0 | 0.2 | 88 | 10.7 | 0.3 | 227 | 259 |
| 0.5 M – 0.8SB | 68 | 3.4 | 0.3 | 5 | 12.8 | 0.1 | 73 | 76 |
| OPC – 0.5WB | 312 | 1.5 | 0.6 | 74 | 1.9 | 0.5 | 386 | 445 |

and the non-reactive part of the binder was not taken into account in these extrapolation models (Snellings et al., 2021; Caron et al., 2023). Therefore, the actual value of $Q_{max}$, at an infinite time would be significantly higher than the values presented in Table 3. For comparison purpose, in this study, the extrapolation of cumulative heat releases up to an age of 28 days was considered.

The maximum heat release , $Q_{max}$, obtained through extrapolation techniques, varies for different S/B ratios and molarity concentrations of the alkaline activator, as shown in Table 3. The concentration of the activator plays a critical role in regulating the chemical reactions that occur during the reaction process, thereby influencing the formation of specific reaction products. Since each chemical reaction has a unique reaction enthalpy, the variations in enthalpy changes translates in different maximum heat release for different mixtures.

### 3.2. Compressive strength evolution

The plot shown in Fig. 5 (a) displays the average development of compressive strength across all the examined mixtures. Samples containing NaOH concentrations of 8 M and 2 M exhibited a significant development in compressive strength within the initial first few hours following casting, registering 4 MPa of strength at 3.5 and 8 h, respectively. The fast development in strength during early ages (within 3 days) was followed by a gradual and steady improvement in later ages. The 8 M – 0.5SB mixture displayed superior compressive strength both in the early and later stages, surpassing the samples with lower molarity concentrations. This observed trend aligns with expectations, as the molarity concentration of the activator significantly impacts the development of strength at early stages. A higher molarity concentration creates a more alkaline environment, characterized by an elevated $Na_2O$ content, which facilitates greater dissolution of the slag binder and subsequent formation of reaction products, ultimately leading to enhanced strength development (Gebregziabiher et al., 2016; Krizan and Zivanovic, 2002). In addition to the high molarity concentration, which contributes to increased strength, the lower water-to-binder (W/B) content also played a crucial role in achieving high early-age compressive strength in the 8 M mix compared to the 2 M and 0.5 M mixes, all with a fixed S/B ratio of 0.5. The lower W/B content resulted in a higher solid volume fraction, enabling the rapid formation of reaction products. This, in turn, facilitated the development of a denser microstructure, leading to a significant and rapid increase in strength

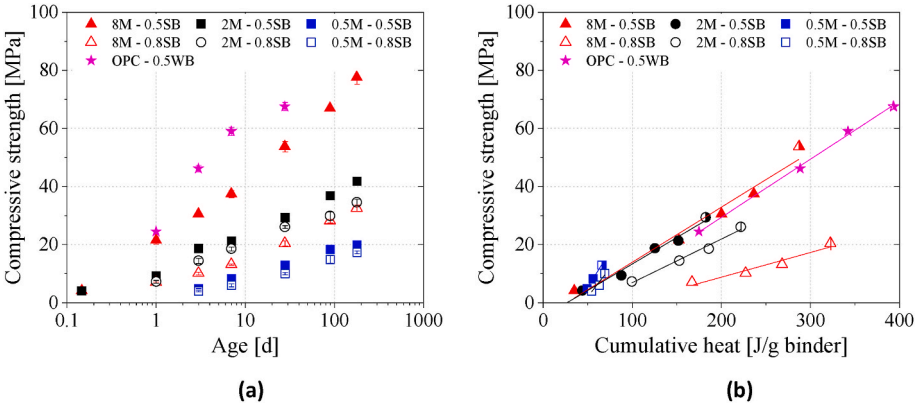


**Fig. 5.** Compressive strength development as a functions of sample age **(a)** and the cumulative heat release **(b).**

over time (Naqi et al., 2023). While the 8 M and 2 M mixtures, activated with a fixed S/B ratio of 0.5, demonstrated relatively high early strength gain, the rate of strength development decreased at later ages, specifically beyond 28 days. The 0.5 M − 0.5SB sample did not exhibit measurable compressive strength initially after 1 day, but experienced an approximate increase of 60–65 % in compressive strength between 7 and 28 days, and around 150 % compared to the 7-day strength, at 180 days of hydration.

The OPC mixture demonstrated the highest compressive strength value of 24.40 MPa after 1 day of testing, surpassing both 8 M and 2 M samples. Moreover, it maintained its strength increment over slag-based mixtures even at later ages. In the case of mixtures featuring a 0.8 S/B ratio, the 2 M − 0.8SB mixture exhibited higher compressive strength than the counterpart with a higher molarity concentration (8 M). This is noteworthy since the former had a lower molarity concentration of 2 M and a higher W/B content of 0.74, while the latter had a molarity concentration of 8 M and a W/B ratio of 0.60. This observation can be attributed to the excessive alkali content present in the 8 M mixture, accounting for 15.61 % ($Na_2O$/slag), in contrast to 4.61 % in the 2 M mixture. Previous reports (Wang et al., 1994) had indicated that an optimal alkali dosage ($Na_2O$ content) within the range of 2 %–5.5 % was effective in achieving the desired material properties. However, increasing the alkali content beyond 5.5 % did not yield a significant effect on strength development (Dai et al., 2022; Reddy and Subramaniam, 2020). In addition, it was observed that excessive alkalinity, denoted by a $Na_2O$ content greater than 9 %, could lead to issues such as efflorescence and brittleness. This was primarily from the presence of free alkali within the system, which had adverse effects on the overall performance and durability of the material (Wang et al., 1994; Saludung et al., 2021). Therefore, it can be deduced that there exists a threshold value for alkali content within a fixed S/B ratio, significantly influencing the strength development of slag-based systems. This also suggests a diminishing influence of W/B content.

In Fig. 5 (b), a linear correlation between compressive strength ($f_c$) and cumulative heat release (Q) is observed. The resulting linear fits reasonably capture the observed strength development. For example, 2 M − 0.5SB sample was specifically chosen for analysis and extrapolation. The process of data fitting yielded a linear equation characterized by a slope of 0.182 MPa/(J/g binder), an intercept of −5.04 MPa, and an $R^2$ value of 0.98. The negative intercept implies that a certain amount of heat release was essential for the formation of reaction products and the initiation of an interconnected network, preceding the compressive strength development (Bentz et al., 2012). This required minimum heat release was indicated with $Q_o$. Additionally, mixtures with higher W/B ratios required a greater amount of heat release to establish a connected network of reaction products and initiate the progression of strength development. This phenomena could be attributed to the increased interparticle spacing resulting from the higher W/B ratio (Bentz et al., 2009; Ismail et al., 2011).

### 3.3. Evolution of elastic and creep properties

#### 3.3.1. Unloading (elastic) modulus ($E_{un}$)

The evolution of unloading (elastic) modulus is visually presented in Fig. 6 (a). Among the AAM samples prepared with a S/B ratio of 0.5, there was a noticeable decrease in modulus with decreasing molarity concentrations. Remarkably, within 10 h following the sample production, the 8 M − 0.5SB mixture demonstrated significant modulus development, reaching around 21 GPa. This value was approximately 60–65 % higher than the modulus of the 2 M − 0.5SB mixture at the same age. This early high modulus was expected, as the increased molarity concentration of the mixture facilitated higher slag dissolution and the formation of a larger amount of dense reaction product, resulting in rapid microstructural development (Gebregziabiher et al., 2016; Ben Haha et al., 2011). Nevertheless, the modulus evolved slowly after 1 day for the 8 M − 0.5SB mixture. During the interval between 1 and 7 days, there was merely 16 % increment in stiffness. The stiffness then stabilized in later stages, showing relatively a modest 13 % increment in stiffness between 7 and 180 days. This phenomenon can be attributed to the high reaction rate during the initial stages, characterized by rapid dissolution of slag. This process resulted in the formation of a dense outer reaction product as well as a thin inner protective layer surrounding the slag grains. The presence of this inner protective layer posed a barrier to the diffusion process, causing the reaction products to continually accumulate around the hydrating slag grains. (Gebregziabiher et al., 2015, 2016; Ben Haha et al., 2011; Deir et al., 2014; Gruskovnjak et al., 2006). At later stages, the ionic diffusivity was reduced due to the increased density of the thin shell of the reaction product, particularly pronounced at higher molarity concentrations (Gebregziabiher et al., 2015). This constrained diffusion process resulted in a marginal stiffness increase during the later stages.

Moreover, for the same S/B ratio of 0.5, higher molarity concentrations corresponded to lower W/B ratios. This reduction in W/B ratio might lead to a reduction in ion mobility, consequently contributing to the deceleration in stiffness development in the later stages (Gebregziabiher et al., 2015). A relatively steady increase in stiffness was observed for the 2 M − 0.5SB mixture, demonstrating a 24 % increase in modulus between 1 and 7 days. However, the rate of stiffness development slowed down in later ages, with an 18 % increment between 7 and 28 days, followed by an approximate 22 % increase after 180 days in comparison to the 7-day value. For the 0.5 M − 0.5SB mixture, modulus testing was not conducted at early ages due to the brittle nature of the sample. No measurable modulus value was obtained until 3 days, at which point the sample displayed a high modulus of 10 GPa. From 3.5 to 7 days, the modulus increased by 19 %. Following this, the sample experienced an increase of approximately 20–25 % in modulus between 7 days and 28 days, followed by a substantial 50–55 % increase after 180

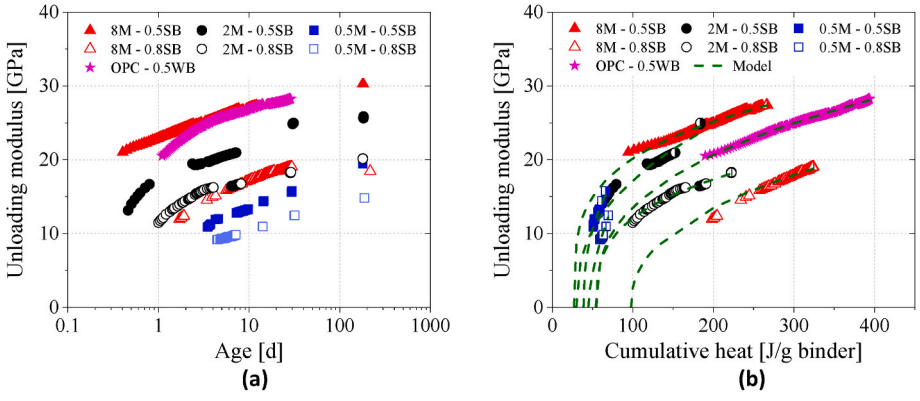


**Fig. 6.** Evolutions of the unloading moduli as a function of sample age **(a)** and the cumulative heat release **(b).**

days when compared to the 7-day value. The OPC mixture exhibited a stiffness development of 20.5 GPa at 1-day testing period, which was 13 % lower value than the corresponding value of 8 M − 0.5SB at the same age. However, rate of stiffness development in the OPC mixture was found to be faster compared to the slag-based 8 M mixture, as indicated by the similar stiffness values of both mixtures at 7 and 14 days.

Among the mixes with a higher S/B ratio, the 2 M − 0.8SB sample demonstrated a higher modulus compared to the 8 M − 0.8SB mix up to 3 days. This observation could be explained by the excessive alkali content present in the 8 M − 0.8SB sample, which hindered the development of stiffness at an early age. However, both mixes showed a similar evolution of stiffness from 3 days up to 28 days. It is noteworthy that the 8 M − 0.8SB sample exhibited a decrease in stiffness at 180 days. This decline in stiffness at later ages for alkali-activated slag mixtures has also been reported in previous studies, attributed to changes in curing conditions and the leaching of ions, which compromised the microstructure of the sample (Lura et al., 2001; Prinsse et al., 2020; Li et al., 2020). In this study, however, all samples were sealed and treated under the same curing regime, indicating that environmental changes were not the main reason for the decrease in stiffness in a specific mixture. However, the excessive high alkali content of 15.61 % ($Na_2O$/slag) in the 8 M − 0.8SB mixture resulted in the formation of whitish deposits (efflorescence) on the sample surface. This occurrence was attributed to the leaching of free alkalis from the sealed sample, which reacted with atmospheric $CO_2$ (Saludung et al., 2021). The loss of structural ions and the formation of crystal growths have been reported to cause a damage to the microstructure of the sample (Saludung et al., 2021; Li et al., 2020), compromising the development of stiffness at later ages. As a result, the data obtained for the 8 M − 0.8SB sample at 180 days was excluded from further discussions.

The 0.5 M − 0.8SB sample reached an unloading modulus of 9 GPa after 4 days, which gradually increased to 9.8 GPa after 7 days. An approximately 27 % increase in stiffness was observed between 7 and 28 days, and approximately 50–55 % increase after 180 days compared to the stiffness at 7 days. Among all other mixtures, the samples with the lowest molarity concentrations, 0.5 M, exhibited the highest rate of stiffness increment between 7 and 180 days. After 180 days, the unloading modulus of the most concentrated mixture, 8 M − 0.5SB with a W/B ratio of 0.37, was only twice as high as the stiffness of the least concentrated mixture, 0.5 M − 0.8SB with a W/B ratio of 0.78. Fig. 6 (b) shows a correlation between the unloading modulus and cumulative heat release. At the same cumulative heat release, samples with higher molarity concentration and lower W/B ratio displayed higher stiffness. The OPC sample, on the other hand, required a higher amount of heat release to reach comparable stiffness to the AAM mixtures with a S/B ratio of 0.5. Samples prepared with 0.8 S/B ratio (0.5 M, 2 M, and 8 M) exhibited lower elastic modulus—for the same amount of heat release—compared to their counterparts prepared at 0.5 S/B ratio. This difference in modulus can be attributed to the substantially higher water content (higher W/B ratio in 0.8 S/B samples), which increases the interparticle spacing between slag grains and requires more heat release to develop stiffness. To model the evolution of unloading moduli $E_{un}$ as a function of cumulative heat release Q, a power function of the form (Eq. (14)) was used.

$$E_{un}(Q) = E_{\infty} \bullet \left(\frac{Q - Q_o}{Q_{max} - Q_o}\right)^{\beta} \quad (14)$$

The model was fitted to the experimental data (see Fig. 6 (b)), where $E_{\infty}$ is the unloading moduli when Q is equal to $Q_{max}$, $Q_o$ denoting minimum heat release required to initiate the stiffness development and β representing the power-law exponent. Numerical values for the fitting parameters along with the root mean square error (RMSE) are provided in Table 4.

It is important to mention that the ultimate unloading moduli $E_{\infty}$ were obtained using least square method. The process of fitting depends strictly on the quantity of points used for fitting, and even more importantly, on the range of cumulative heat release (Q) within which the fitting is conducted. However, smaller RMSE values suggest that the model fits well within the actual data and effectively describes the stiffness evolutions throughout the reaction process.

**Table 4**
Unloading modulus $E_{un}$ parameters for all slag based compositions and OPC mixture.

| Mix ID | $E_{\infty}$ (GPa) | $Q_o$ (J/g) | $Q_{max}$ (ISR) (J/g) | β (−) | RMSE (GPa) |
|---|---|---|---|---|---|
| 8 M − 0.5SB | 29.23 | 27 | 338 | 0.25 | 0.23 |
| 2 M − 0.5SB | 25.36 | 30 | 214 | 0.40 | 0.74 |
| 0.5 M − 0.5SB | 17.38 | 39 | 77 | 0.41 | 0.28 |
| 8 M − 0.8SB | 20.60 | 98 | 380 | 0.43 | 0.50 |
| 2 M − 0.8SB | 19.23 | 55 | 259 | 0.31 | 0.27 |
| 0.5 M − 0.8SB | 14.11 | 45 | 76 | 0.62 | 0.26 |
| OPC – 0.5WB | 29.50 | 54 | 445 | 0.37 | 0.09 |

### 3.3.2. Poisson's ratio

The temporal evolution of Poisson's ratio is shown in Fig. 7. The inability to present the Poisson's ratio evolution for all the tested mixtures resulted from the malfunction in one of the lateral displacement sensors after a few tests. As a result, Poisson's ratio data for OPC mix was sourced from a prior study (Delsaute, 2016) for comparison with the results of select AAM mixtures, as shown in Fig. 7 (a). The Poisson's ratio for the OPC-based mixture demonstrated a decrease to an approximate value of 0.13 during the early stages of the reaction, followed by an increase to a value near to 0.18. This initial decrease in Poisson's ratio was linked to the presence of a continuous water phase that gradually became discontinuous due to water consumption during the hydration process. Once the matrix reached the percolation threshold, solid stiffening dominated the process, resulting in an increase in Poisson's ratio (Bernard et al., 2003). In contrast, the 8 M − 0.5SB specimen maintained a constant Poisson's ratio of roughly 0.13 throughout the testing duration. This phenomenon is attributed to the rapid dissolution of slag during the initial stages, resulting in the formation of a dense outer reaction product layer. At later stages, the ionic diffusivity was reduced due to the increased density of the thin shell of the reaction product, particularly pronounced at higher molarity concentrations (Gebregziabiher et al., 2015). Consequently, the combination of fast initial formation of reaction products followed by reduced refinement at later stages leads to a matrix with a constant value of Poisson's ratio from the early stages.

Conversely, for specimens with the same S/B ratio of 0.5, the Poisson's ratio of the 0.5M-0.5SB sample did not exhibit a constant trend during the hardening process. Initially, it decreased from 0.18 to approximately 0.10, then gradually increased to a final value close to 0.13. The differing evolution of Poisson's ratio between the 8 M and 0.5 M mixtures, both prepared with the same S/B ratio of 0.5, can be attributed to two factors. Firstly, the higher molarity concentration in the 8 M mixture facilitates a faster dissolution of the binder, resulting in a dense microstructure at early stages. This density keeps the Poisson's ratio almost constant from the very early age. Secondly, the 8 M mixture has a lower W/B content compared to the 0.5 M mixture, with W/B ratios of 0.37 and 0.49, respectively. This reduction in the W/B ratio in the 8 M mixture likely leads to decreased ion mobility and, consequently, contributes to lesser microstructure refinement at later stages.

Among mixtures with a 0.8 S/B ratio, the 8 M − 0.8SB mixture initially displayed a slightly lower Poisson's ratio of 0.10. This value increased to a final measurement of 0.13 at later stages. The subtle evolution in Poisson's ratio in the early stages can be attributed to the relatively higher W/B ratio of 0.60, as opposed to the 8 M − 0.5SB mixture, which had a W/B ratio of 0.37. These observations align with the reported average range of Poisson's ratios (0.12–0.16) for alkali-

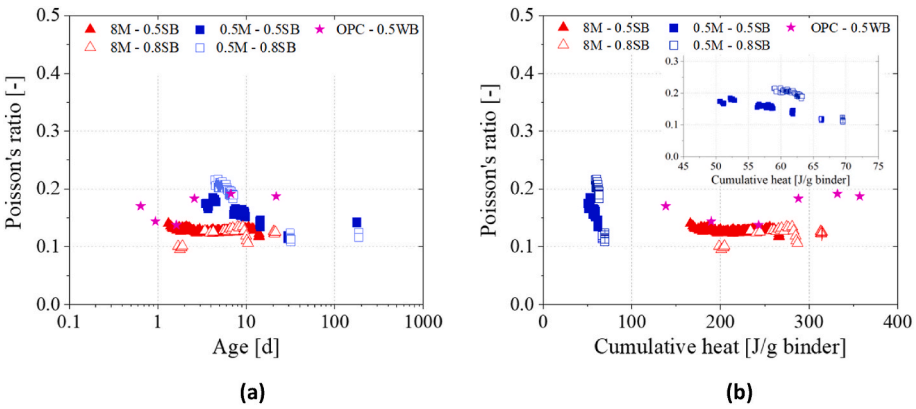


**Fig. 7.** Evolutions of the Poisson's ratios as a function of sample age **(a)** and the cumulative heat release **(b).**

activated systems found in the literature (Hardjito, 2005; Diaz and Allouche, 2010; Thomas and Peethamparan, 2015). On the other hand, the 0.5 M – 0.8SB mixture exhibited a gradual decrease in Poisson's ratio from 0.20 to approximately 0.10. It then gradually increased to a final value close to 0.12. This trend in the 0.5 M mixtures can be elucidated by their lower alkali content and higher W/B ratio, leading to a slower rate of stiffness development, as discussed in previous sections.

Fig. 7 (b) illustrates the correlation between Poisson's ratio and cumulative heat release. For clarity, the correlation for the low concentrated mixtures (0.5 M) at lower cumulative heat is presented in the inset of Fig. 7 (b). It can be seen that the value of Poisson's ratio gradually decreased as the heat release increased for the low molarity mixtures, whereas the high molarity mixtures maintained a relatively constant Poisson's ratio with minimal fluctuations. In comparison, the OPC mix exhibited a higher Poisson's ratio at higher cumulative heat compared to the AAM mixtures.

### *3.3.3. Creep parameters ('A' and 'K') and creep prediction error*

Fig. 8 (a) shows the temporal evolutions of the creep amplitude parameter 'A'. Across all compositions, the amplitude parameter exhibited a decreasing trend during the hardening phase. This gradual decrease in the amplitude parameter signifies a reduction in the creep activity of the mixtures (Carette and Staquet, 2016). Among the samples prepared with a S/B ratio of 0.5, the 8 M sample displayed nearly unvarying amplitude value of 0.10 from the first creep test up to 10 days, followed by a marginal dip at an age of 14 days, ultimately reaching 0.07 at 180 days. On the other hand, the 2 M mixtures exhibited a significant decay in amplitude from 0.20 at first creep test at an age of 11 h to 0.06 for the last creep cycle at an age of 180 days. The amplitude of the 0.5 M mixtures, compared to the 2 M and 8 M mixtures with the same S/B ratio, experienced a more steady decrease in amplitude from 0.10 at first creep test to 0.04 at the last creep test at an age of 180 days. This implies that at an age of 180 days, the creep strains account for roughly 7 %, 6 %, and 4 % of the elastic strains following only a 5-min stress plateau during the short-term creep cycle for the 8 M, 2 M, and 0.5 M mixtures, respectively, prepared with a S/B ratio of 0.5. The reference mixture prepared with OPC exhibited a decay in amplitude from 0.11 at the first creep test at an age of 1 day to 0.05 for the last creep test at an age of 28 days. It is worth noting that the amplitude parameter was found to be lower for mixtures prepared with a higher W/B ratio, as shown in Table 2, which aligns with prior findings (Delsaute, 2016).

The trend remained the same for mixtures with a S/B ratio of 0.8. The higher molarity mix (8 M) maintained an almost constant amplitude parameter value of 0.10 until the final creep test at 28 days. In contrast, the 2 M mixture exhibited a gradual decline in amplitude over time, decreasing from 0.12 at first creep test at the age of 1 day to approximately 0.06 for the last creep test at an age of 180 days. The 0.5 M sample, mixture with the lowest molarity concentration and a W/B ratio of 0.78, displayed a notable scattering of the amplitude values, that started at 0.09 for the first creep test at an age of 4.4 days to 0.05 for the last creep test at an age of 180 days. Consequently, at a 180-day age, the creep strains accounted for roughly 6 %, and 5 % of the elastic strains after only a 5-min stress plateau during the short-term creep cycle for the 2 M and 0.5 M mixtures, respectively, prepared with a S/B ratio of 0.8. A correlation between the amplitude parameter and cumulative heat release is presented in Fig. 8 (b). The amplitude parameter for high molarity (8 M) mixtures maintained a stable range around 0.09 to 0.10 for the given heat release up to 28 days. However, for the 2 M and 0.5 M mixtures, a gradual decay in the amplitude parameter was observed with increasing heat release. In contrast, the OPC sample required a higher amount of heat release to reach amplitude values comparable to the 2 M mixtures. The inset in Fig. 8 (b) illustrates the lower cumulative heat

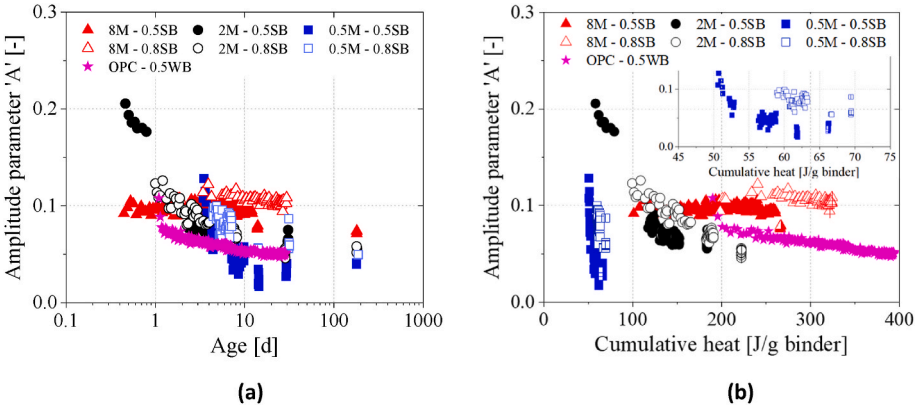


**Fig. 8.** Evolutions of the amplitude creep parameters 'A' as function of sample age **(a)** and the cumulative heat release **(b).**

release for the 0.5 M mixture.

The evolution of the kinetic parameter, denoted as K, with increasing age is graphically represented in Fig. 9 (a). The higher molarity mixtures (8 M) showed a relatively stable trend in the kinetic parameter, exhibiting minor fluctuations while largely maintain a value close to 0.4. In contrast, within the intermediate molarity range mixtures (2 M), the mixture with a S/B ratio of 0.5 showed a decrease in kinetic parameter from 0.5 at an age of 11 h to 0.3 at the last creep test at an age of 180 days. For the 2 M − 0.8SB mixture, the kinetic parameter reduced from 0.6 at an age of 1 day to 0.4 at the last creep test at an age of 180 days. On the other hand, compositions with lower molarity concentrations (0.5 M) displayed a significant drop in the kinetic parameter, from 0.7 at an age of 3 days to approximately 0.4 at the last creep test at an age of 180 days. Interestingly, all tested AAM mixtures exhibited a value close to 0.4 at an age of 180 days, indicating a consistent and molarity-independent characteristic. Similarly, the kinetic parameter for the OPC mixture decreased from 0.5 at the first creep test at an age of 1 day to 0.4 at the last creep test at an age of 28 days, aligning with the existing literature (Delsaute et al., 2016a).

The corelation between the evolution of the kinetic parameter and cumulative heat release is illustrated in Fig. 9 (b). Notably, the 2 M and 8 M mixtures showed a good correspondence, indicating a similar range of the kinetic parameter for the same amount of heat release. Likewise, the OPC mixture displayed a comparable range of the kinetic parameter to that of 2 M and 8 M mixtures. Conversely, low molarity mixtures (0.5 M) showed a significant decay in the amplitude parameter within a very limited amount of heat release. A closer examination of the correlation between the kinetic parameter and heat release for the 0.5 M mixtures is presented in the inset of Fig. 9 (b).

The creep prediction error, also known as the residual strain error, is obtained by comparing experimentally measured strains with modelled strains and is plotted as a function of age and cumulative heat release in Fig. 10 (a) and (b), respectively. Among the high molarity mixtures, 8 M and 2 M displayed a continuous decay in creep error over time, indicating a better model fit during the hardening phase, characterized by the minimal dispersion of data. However, mixtures prepared with lowest molarities, specifically 0.5 M with 0.5 SB and 0.8 SB did not exhibit a consistent trend in the progression of creep error. Instead, they showed relatively higher scattering of residual strains during the initial stages (up to 10 days), followed by the reduced residual strains at later ages. Fig. 10 (b) illustrates the relationship between creep error and cumulative heat release. For the same amount of heat release, all mixture demonstrated a comparable creep error, except 0.5 M mixtures. In these low mixtures with low molarity (0.5 M), which generated comparatively less amount of heat, a higher scattering of predicted creep error was observed during the hardening process. A closer look at the temporal decrease in creep error for the 0.5 M mixtures is shown in the inset of Fig. 10 (b).

## 4. Discussion

### 4.1. Evolution of the total strains

The creep behaviour of the mixtures was further analysed by comparing the experimentally obtained total strains with the modelled total strains, using a power-law creep function characterized by two parameters, ‘A’ and ‘K’. Fig. 11 displays the total strain histories of a single creep test cycle for each AAM mixture, recorded at a 7-day age. The results apparently indicate a promising fit of the model to the actual measurements.

Nonetheless, upon a closer examination of the interface between the elastic and viscous regions, particularly at the end of the loading branch (that corresponds to the apparent elastic region) and the start of the stress plateau (which represents the viscous region), an overshooting of the elastic strains was observed. This observation is illustrated in the amplified portion of Fig. 12 and indicates that the modulus derived from the unloading branch of the creep test cycle underestimated the actual elastic modulus of the material. This discrepancy is attributed to the development of short-term creep strains during the loading and unloading stages of the test (Irfan-Ul-Hassan et al., 2016). In order to capture the overshot elastic strains, an improved fitting of the power-law function was performed by increasing the unloading modulus by a few percent, typically ranging between 6 % and 8 %. This adjustment allowed for a more accurate estimation of the unloading modulus. The approach of using larger estimates of the unloading modulus has been reported in the existing literature (Irfan-Ul-Hassan et al., 2016; Göbel et al., 2018b; Königsberger et al., 2021). By incorporating this improved estimate of the unloading modulus, the three-parameter power-law function (‘E’ - the improved modulus, ‘A’, and ‘K’) demonstrated an improved fit to both the elastic and viscous strains. This enhancement is illustrated in the amplified portion of Fig. 12.

It’s noteworthy that this adjustment in the unloading modulus had a notable influence on the development of the amplitude creep parameter ‘A’ and the kinetic creep parameter ‘K’. Hence, in the following section, a comprehensive comparison was conducted concerning the progressions of both elastic and viscoelastic properties. This comparison highlights the utilization of the conventional two-parameter power-law creep function (‘A’ and ‘K’), alongside an improved version of creep function, which incorporates three parameters (‘E’, ‘A’, and ‘K’). The purpose was to more accurately capture the strains determined through experimental means.

#### 4.1.1. Comparative analysis of conventional and improved power-law type creep function on the evolutions of creep properties

The temporal evolutions of classical moduli values, obtained from the unloading branch of the creep test, are shown in Fig. 13 (a). In Fig. 13 (b), an improved estimate of the unloading moduli, typically 6

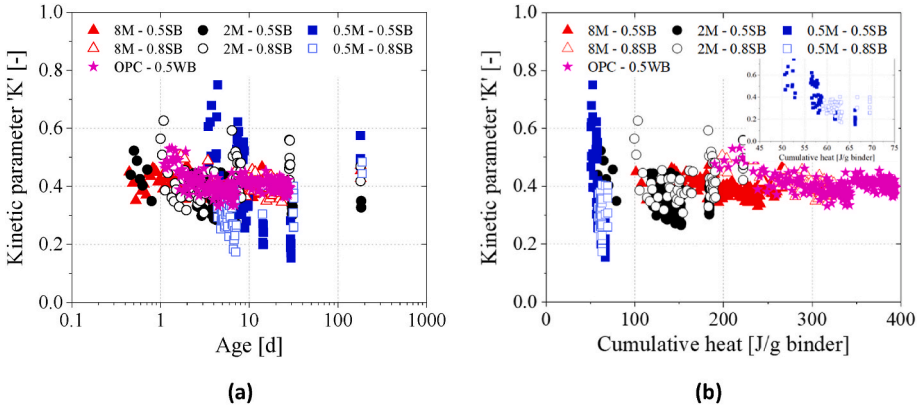


**Fig. 9.** Evolutions of the kinetic creep parameters ‘K’ as function of sample age **(a)** and the cumulative heat release **(b).**

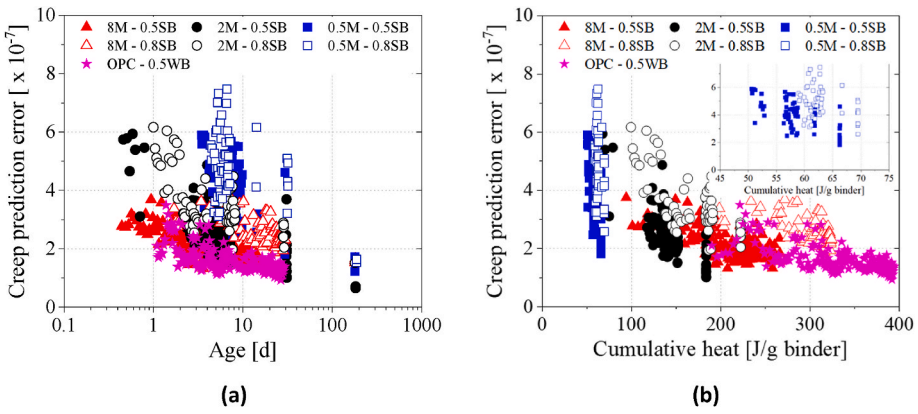


**Fig. 10.** Evolutions of the creep errors as function of sample age **(a)** and the heat release **(b).**

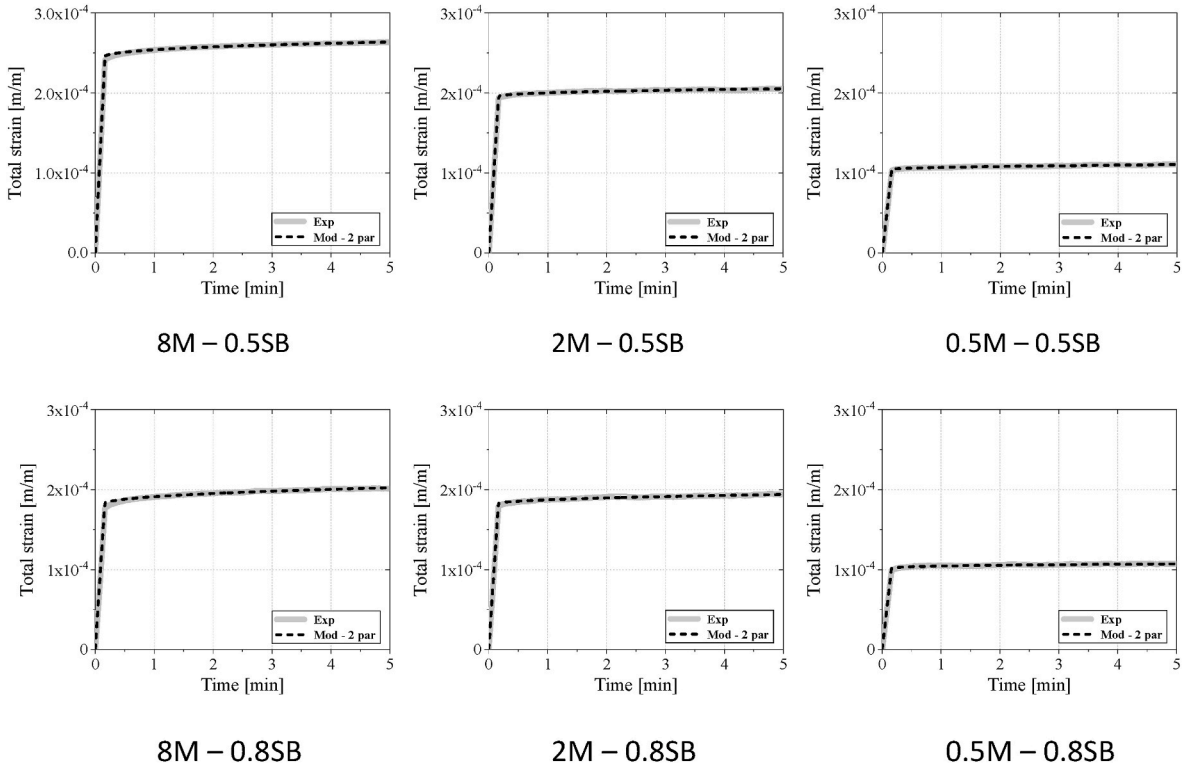


**Fig. 11.** Total strain histories of one creep test cycle for all six slag based mixtures at an age of 7 days: the grey solid line refer to the experimentally obtained strains, while black dashed lines to the power-law model fit utilizing 2 parameters, amplitude 'A' and kinetic 'K', see section 3.3.3.

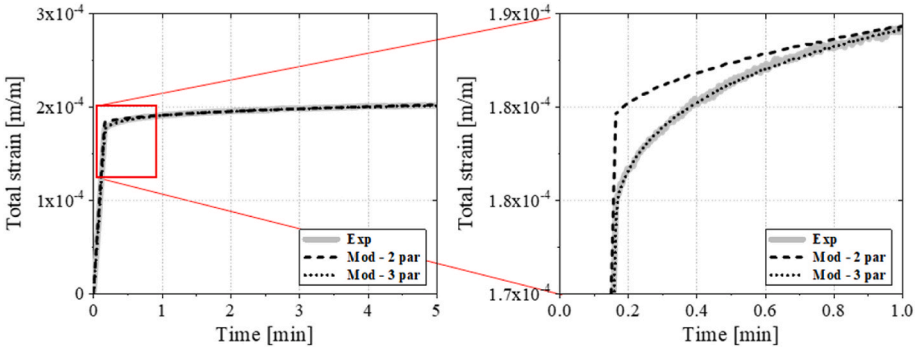


**Fig. 12.** Experimentally obtained total strain evolution; from one short-term creep cycle, and corresponding conventional and improved power-law model fit using 2 parameters 'A' and 'K' and three parameters 'E', 'A', and 'K' and magnified region highlighting the best fit for mixture 8 M − 0.8SB at an age of 7 days.

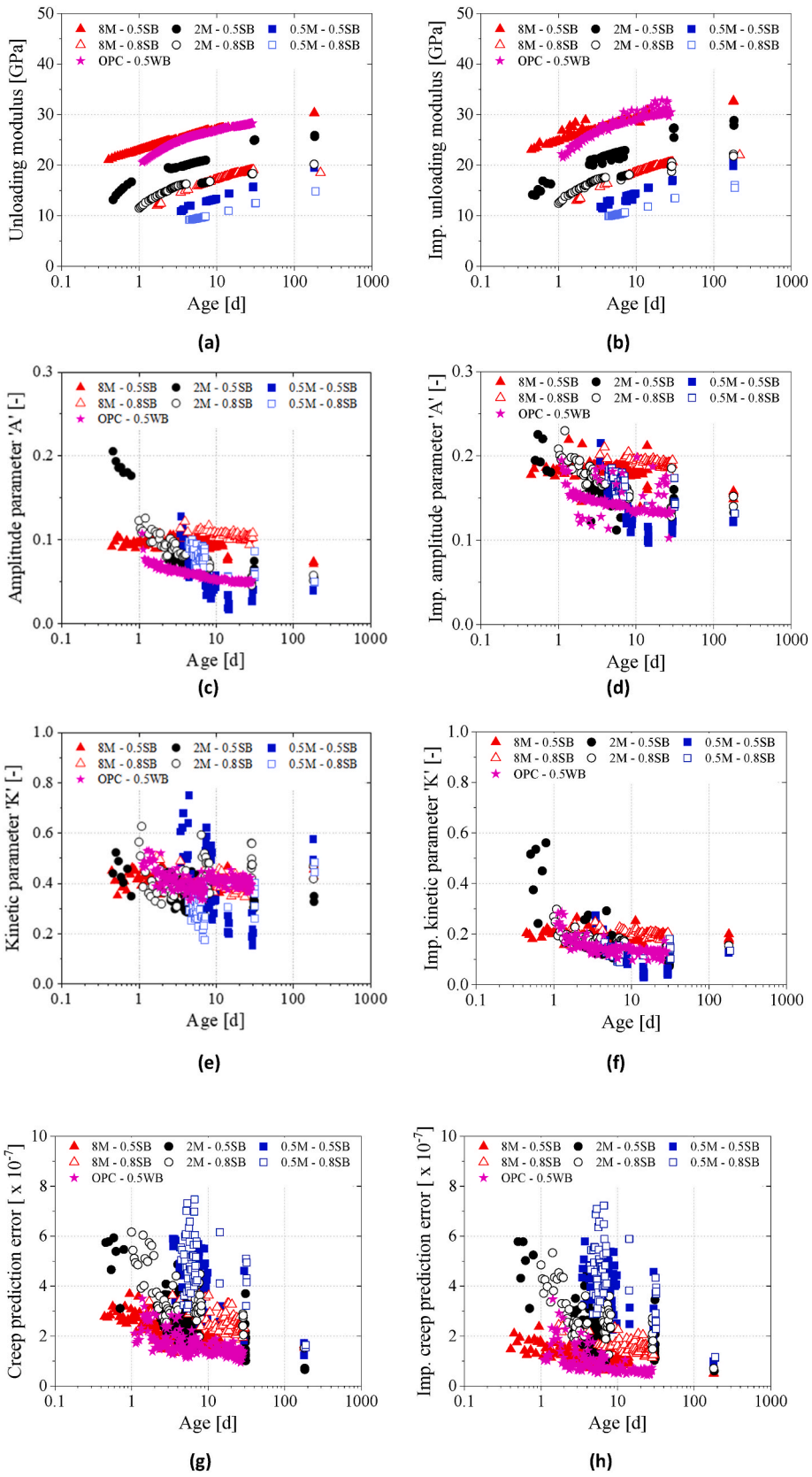


**Fig. 13.** Comparison between typical and improved evolutions of the unloading moduli **(a)** and **(b)**, the amplitude creep parameter 'A' **(c)** and (d), the kinetic creep parameter 'K' **(e)** and **(f)**, and the creep prediction error **(g)** and **(h)** as a function of sample age.

%–8 % higher, is highlighted. These enhanced estimates of moduli aim to mitigate the overshooting of elastic strains, as discussed in the previous section. For each 5-min plateau of stress in the short-term creep test, the creep coefficient was modelled using a power-law type creep function (equation (8)) with two parameters, 'A' and 'K'. The evolutions of the amplitude parameter 'A' obtained using this conventional power-law function is shown in Fig. 13 (c). The amplitude parameter decreased from its peak value of 0.20 (2 M − 0.5SB) at first creep test at an 11-h age and reached 0.04 (0.5 M − 0.5SB) for the last creep cycle at an age of 180 days. This indicates that the contribution of creep strains to the overall elastic strains is only around 4 % following a 5-min stress plateau, based on the last test conducted at 180 days. on the contrary, with the improved model fitting, amplitude parameter resulted in higher values across all ages, as illustrated in Fig. 13 (d). The amplitude decreased from a maximum value of 0.23 (2 M − 0.5SB) at the first creep test at an age of 11 h to a minimum value of 0.12 (0.5 M − 0.5SB) at the last creep test at an age of 180 days. This suggests that creep strains account for approximately 12 % of the elastic strains after only 5 min of loading force at 180 days. Therefore, a significant difference in the amplitude creep parameter 'A' is observed when comparing the conventional and improved fitting of the model to the measurements. The kinetic creep parameter 'K' decreased from a peak value of 0.7 (0.5 M − 0.5SB) at an age of 3 days to approximately 0.4 at the last creep test at an age of 180 days, as depicted in Fig. 13 (e). Notably, the 'K' value exhibited greater dispersion of data during the test cycles for the 0.5 M mixtures. In contrast, with the improved model fitting, a reduced scattering of 'K' values was achieved, ranging from 0.35 at early ages to approximately 0.15 at the last creep test at an age of 180 days, as shown in Fig. 13 (f). These 'K' values aligned with the range of power-law creep exponent β (between 0.20 and 0.25) employed to evaluate creep strains during short durations of loadings (Irfan-Ul-Hassan et al., 2016; Göbel et al., 2018a; Ausweger et al., 2019; Binder et al., 2023; Königsberger et al., 2021). The residual strains obtained from both the typical and improved model fitting are shown in Fig. 13 (g) and (h), respectively. The typical power-law creep function, with two parameters fitting, exhibited a very low creep error, indicating only a slight difference in creep error reduction compared to the improved model fitting using three parameters with the experimentally acquired measurements.

### 4.2. Influence of rate of application of load on the evolutions of elastic and viscoelastic properties

In this test, a constant load equivalent to 20 % of the compressive strength was exerted on the same sample for four distinct loading intervals: 5, 10, 30, and 300 s, occurring every hour. Following a 300-s period of maintaining the force (stress plateau), the load was removed within a 10 s interval. The results depicting the modulus evolution from the "loading" branch for various durations up to 90 days are shown in Fig. 14 (a). The results indicated that increasing the rate of load application had a significant effect on the stiffness evolution of the sample. This effect can be attributed to the increase in strain over time resulting from creep (Neville, 1997). However, as hydration progresses, the influence of the loading rate on stiffness development diminishes as the viscous properties decrease (Delsaute et al., 2016b). These findings align with the outcomes observed by Delsaute et al. (2016b) in OPC-based systems, where a comparable impact of loading rate on modulus evolution was demonstrated. The stiffness progressions derived from the "unloading" branch are highlighted in Fig. 14 (b). Since unloading was performed within 10 s for every cycle, irrespective of the loading rate, a single trend of modulus progression was obtained. This trend implies that the sample remained unaltered even after undergoing numerous cycles with different loading rates.

The progression of temporal decay in the creep amplitude parameter for different loading durations is presented in Fig. 15 (a). There were no notable distinctions in the amplitude parameter across a range of load application rates, spanning from 5 s to 300 s. The amplitude parameter exhibited a decline from 0.06 at the first creep test at an age of 1 day to 0.03 for the final creep test at an age of 94 days. This suggests that the creep strains generated during the loading phase were effectively considered in the evaluation process, leading to an amplitude outcome independent of the rate of load application. Conversely, the kinetic parameter decreased from 0.7 at the first creep test at an age of 1 day to 0.4 at the last creep test at an age of 94 days. Like the amplitude parameter, the kinetic factor remained unaffected by varying loading rates, as illustrated in Fig. 15 (b).

The decline in creep error over time, observed for the varying rates of load application (5 s, 10 s, 30 s, and 300 s), is presented in Fig. 16. A consistent reduction in creep error was noted over time, across different loading rates. This decline can be attributed to the diminishing viscous characteristics of the sample as hydration progresses. Consequently, a more accurate alignment with experimental results is achieved, leading to a decrease in creep error during later stages.

### 4.3. Influence of magnitude of load on the evolutions of elastic and viscoelastic properties

A cyclic test was performed on 2 M − 0.5SB mixture-based sample, starting from 1 day after demoulding. The test involved applying loads corresponding to 5%, 10%, 20%, and 40% of the compressive strength to the sample every hour, with a loading/unloading rate of 10 s and a stress plateau duration as described in section 2.3.3.2 (also see Fig. 2). The evolutions of the measured loading and unloading (elastic) moduli values for different stress ratios are shown in Fig. 17 (a) and (b), respectively. The results indicate that the increasing stress concentration (from 5 % to 40 %) only slightly influenced the measured elastic modulus, particularly at the early age, where higher stress magnitudes

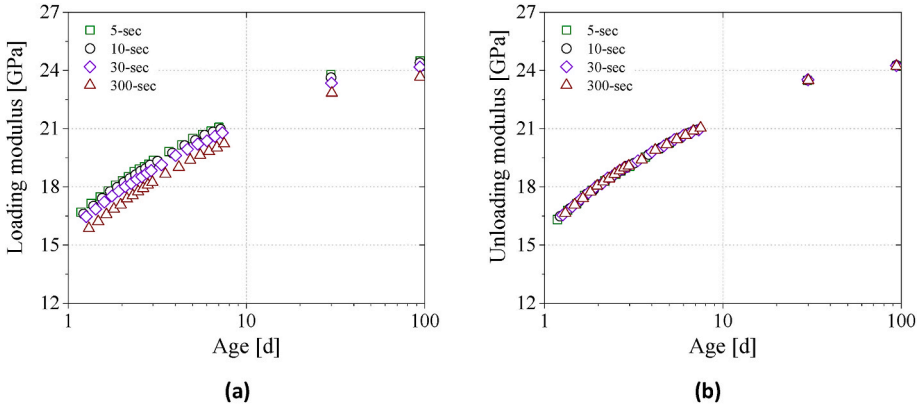


**Fig. 14.** Temporal evolutions of the loading moduli **(a)** and unloading moduli **(b)** for the loading rates of 5, 10, 30 and 300-s.

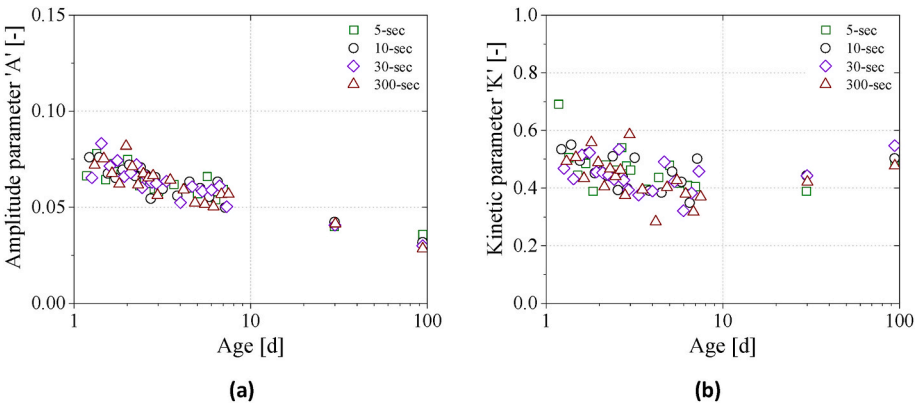


**Fig. 15.** Evolutions of the amplitude creep parameters 'A' as function of sample age **(a)** and the kinetic creep parameter 'K' as function of sample age **(b)** for the loading rates of 5, 10, 30 and 300-sec.

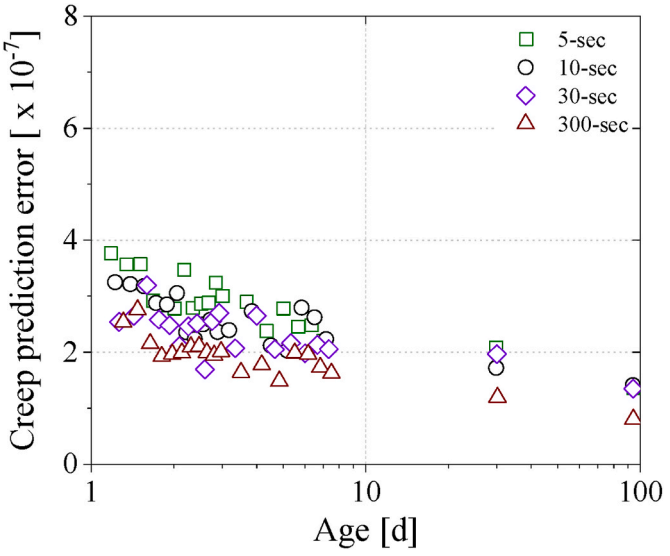


**Fig. 16.** Temporal decay of creep error for the loading rates of 5, 10, 30 and 300-sec.

led to lower modulus values. It is evident that the impact of varying stress magnitudes on modulus evolution can be considered negligible, both in terms of loading and unloading modulus estimations. This finding, however, contradicts the observations made by (Delsaute et al., 2016b) on OPC systems, which demonstrated a significant impact of loading magnitudes on modulus evolution at early ages.

The temporal decay of the amplitude creep parameter 'A' is shown in Fig. 18 (a) for various loading magnitudes of 5 %, 10 %, 20 %, and 40 % of the compressive strength. As expected, higher stress magnitudes resulted in higher amplitudes, with the highest amplitude observed for the 40 % loading magnitude, followed by 20%, 10%, and 5%. This can be attributed to the fact that higher stress magnitudes allowed for greater deformation, leading to higher amplitude values. A comparable observation was documented in a previous investigation of OPC systems (see page 333, Fig. 6 in ref (Delsaute, 2016)). Throughout all the tested cycles, the 40 % stress magnitude produced amplitudes that were twice as high as those produced by the 5% stress loading at all testing ages. For the kinetic creep parameter 'K', the values mostly remained in the range close to 0.4 with some scattering for the lower loading magnitudes of 5% and 10% of the compressive strength, as depicted in Fig. 18 (b).

The residual error for the loading magnitudes of 5 %, 10 %, 20 %, and 40 % of the compressive strength is depicted in Fig. 19. Higher magnitude stress concentrations showed a good decay of creep error over time; the 40 % stress loading depicted the lowest creep error among all tested loading magnitudes. On the contrary, the 5% and 10% loading magnitudes demonstrated a greater difference (creep error) between the experimentally obtained values and the modelled strains; the effect was more pronounced at early ages and diminished as the samples hardened.

### *4.4. Comparative analysis of different evaluation procedures regarding the evolution of elastic and viscoelastic properties*

Herein, a comparison is conducted among the elastic and viscoelastic properties, obtained through three distinct test procedures. The reference point for this analysis is the 2 M − 0.5SB mixture. The evolution of moduli resulting from an identical loading rate (applying the load within

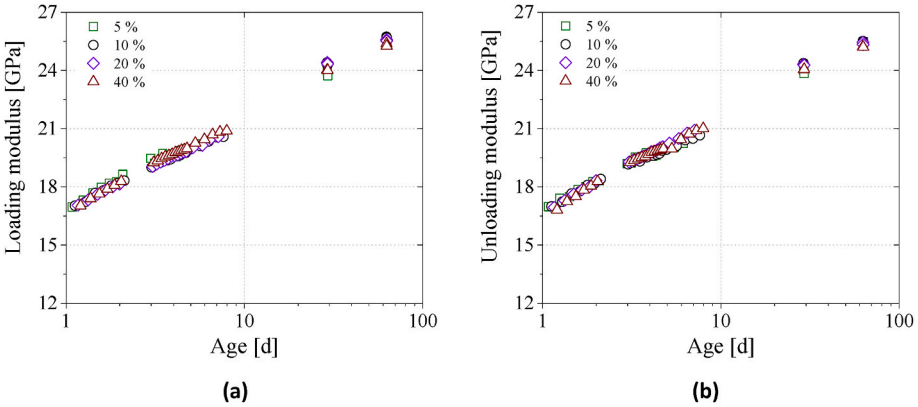


**Fig. 17.** Temporal evolution of the loading modulus **(a)** and unloading modulus **(b)** for the loading magnitudes of 5, 10, 20 and 40% of compressive strength.

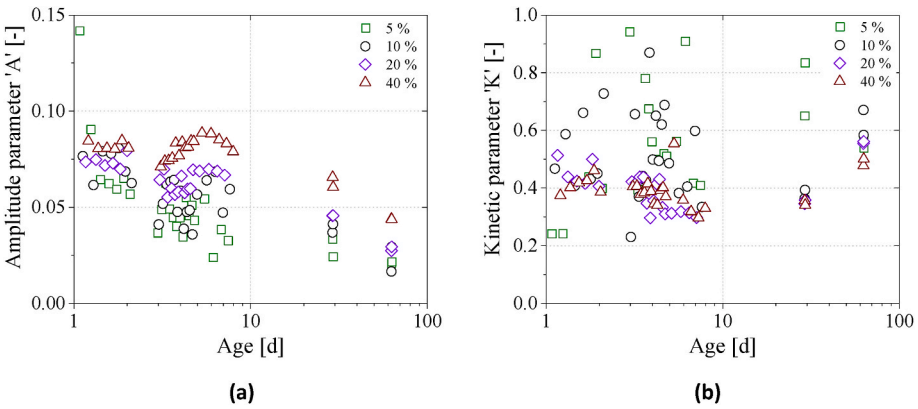


**Fig. 18.** Evolutions of the amplitude creep parameters 'A' as function of sample age **(a)** and the kinetic creep parameter 'K' as function of sample age **(b)** for the loading magnitudes of 5, 10, 20 and 40% of compressive strength.

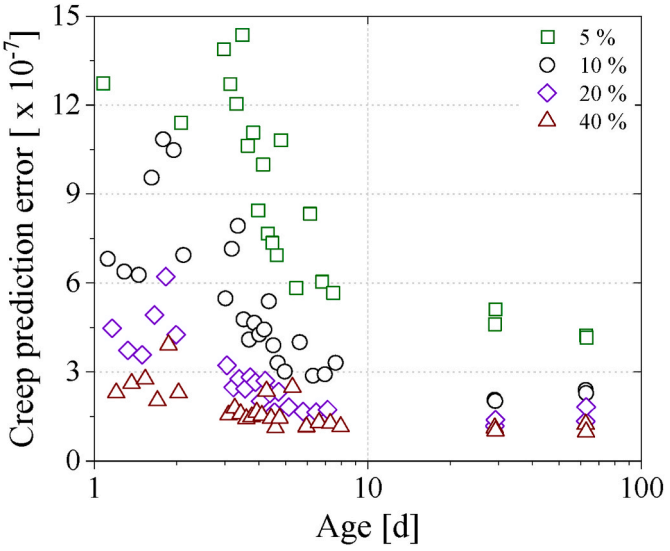


**Fig. 19.** Temporal decay of creep error for varying magnitudes of 5, 10, 20 and 40 % of compressive strength.

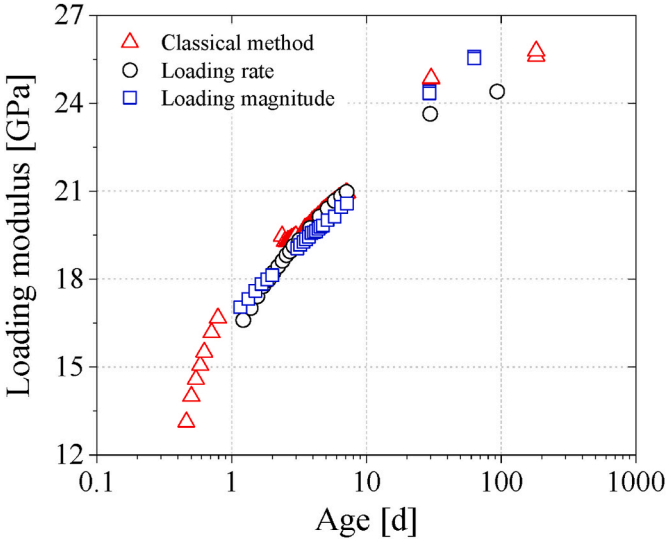


**Fig. 20.** Temporal evolutions of the loading moduli obtained through the classical, loading rate and loading magnitude test procedures for the 2 M – 0.5SB mixture.

10 s) and loading magnitudes (load equivalent to 20% of the compressive strength) is presented. This representation aims to show the repeatability and reproducibility of data as assessed by means of diverse testing methodologies, as illustrated in Fig. 20. Remarkable consistency in the evolution of stiffness was observed across the three distinct testing procedures. During the initial stages, up until a duration of 7 days, no substantial differences in the trajectory of loading moduli were evident. Nonetheless, the moduli values derived from the loading rate testing procedure (section 4.2) exhibited a marginal reduction, around 1–1.5 GPa, in contrast to the values derived from the loading magnitude procedure (section 4.3), which aligned closely with the outcomes from the conventional method (section 3.3). It is worth noting that these slight variations in moduli hold limited significance, given the substantial variations (in terms of stress rate and stress magnitude) in creep cycles introduced by the loading rates and loading magnitudes employed throughout the testing protocol.

Fig. 21 (a) and (b) illustrate the amplitude and kinetic parameters acquired through three distinct testing procedures, respectively. The amplitude parameter decreased in the similar range of 0.06 at an age of 1 day to 0.03 at later stages and, thus, showed good reproducibility across the three testing methods. Similarly, the kinetic parameter displayed a comparable trend, started at 0.5 at the initial stages and decreased to a value near 0.4 at later phases. This trend is consistent across the results obtained from the three different testing approaches.

## 5. Conclusions

A comprehensive experimental campaign, featuring hourly-repeated 5-min creep tests, has yielded valuable quantitative insights into the early-age evolution of elastic stiffness and creep properties in alkali-activated slag-based mortar samples. Based on the experimental findings and associated model fitting, the following conclusions are derived:

- Isothermal calorimetry tests unveil distinct reaction patterns in slag-based systems, with NaOH concentration affecting both initial reaction rates and maximum heat release, diverging from conventional OPC-based materials.
- Higher NaOH molarity concentration accelerates reaction processes, enhancing early-age mechanical properties (strength and stiffness) of slag-based materials. However, an optimal alkali dosage ($Na_2O$ content) is vital for long-term strength development.
- The creep behaviour analysis involves comparing experimentally obtained total strains with modelled strains using a power-law function defined by (A) and (K) parameters. The strain histories demonstrate a favourable fit, yet reveal an overshooting of elastic strains at transition zones. To address this, an improved unloading

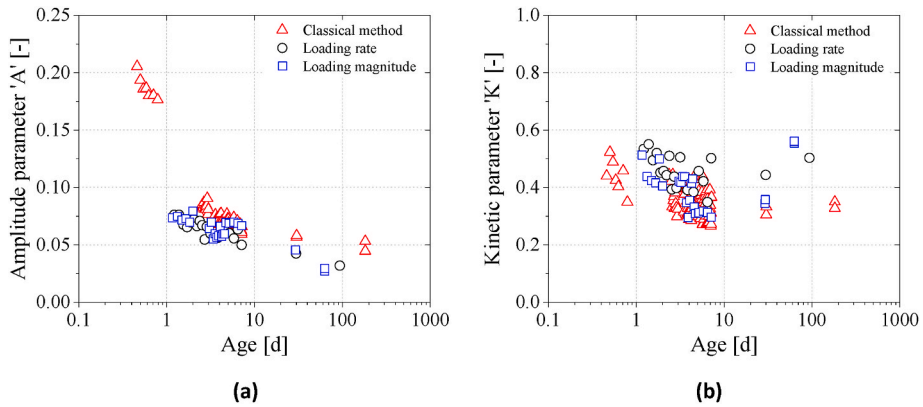


**Fig. 21.** Evolutions of the amplitude creep parameters 'A' as function of sample age **(a)** and the kinetic creep parameter 'K' as function of sample age **(b)**, obtained through the classical, loading rate and loading magnitude test procedures for the 2 M − 0.5SB mixture.

modulus is introduced, leading to an improved fit with a three-parameter power-law function ('E', 'A', 'K'). This refinement is crucial in accurately capturing strains determined through experiments, highlighting the effectiveness of both conventional and improved creep functions.

- The creep amplitude parameter (A) demonstrates a diminishing trend during the hardening phase. This trend varies based on different molarity and S/B ratios. However, the amplitude value remains higher for 2 M and 8 M mixtures compared to OPC mixture. In contrast, the kinetic parameter (K) in AAM mixtures remains steady, hovering around 0.4 in the two-parameter fit and 0.15 in the three-parameter fit, irrespective of molarity concentration — similar to the OPC mixture.
- A constant load at 20 % compressive strength in different intervals (5, 10, 30, and 300 s), every hour, reveals loading rate impact on stiffness evolution, which gradually decreases over time due to reaction advancement. Creep amplitude and kinetic parameters remain unaffected by varying rates.
- Cyclic testing on a 2 M − 0.5SB mixture-based sample reveals minimal influence of varying stress magnitudes (5 %–40 % of compressive strength) on elastic modulus evolution, contrary to OPC systems. Amplitude creep parameter (A) and kinetic parameter (K) remain consistent across loading magnitudes, demonstrating deformation patterns and viscoelastic behaviour.
- The comparison of elastic and viscoelastic properties through various test procedures reveals consistent stiffness evolution and reproducibility of amplitude and kinetic parameters, reaffirming the reliability of the experimental approaches.

## 6. Limitation of the study

This study is limited to slag mortar activated by sodium hydroxide at a curing temperature of 20 °C.

## Declaration of competing interest

The authors declare that they have no known competing financial interests or personal relationships that could have appeared to influence the work reported in this paper.

## Data availability

Data will be made available on request.

## Acknowledgements

This paper is the result of research actions performed in the framework of the FNRS-FWO-EOS project 30439691 'INTERdisciplinary multiscale Assessment of a new generation of Concrete with alkali-activated maTerials' (INTERACT). The financial support by FNRS-FWO-EOS is gratefully acknowledged.

## References

Aboulayt, A., Souayfan, F., Roziere, E., Jaafri, R., Cherki El Idrissi, A., Moussa, R., Justino, C., Loukili, A., 2020. Alkali-activated grouts based on slag-fly ash mixtures: from early-age characterization to long-term phase composition. Construct. Build. Mater. 260, 120510.
Ausweger, M., Binder, E., Lahayne, O., Reihsner, R., Maier, G., Peyerl, M., Pichler, B., 2019. Early-age evolution of strength, stiffness, and non-aging creep of concretes: experimental characterization and correlation analysis. Materials 12, 1–17.
Bakharev, T., Sanjayan, J.G., Cheng, Y.B., 2003. Resistance of alkali-activated slag concrete to acid attack. Cement Concr. Res. 33, 1607–1611.
Bažant, Z.R., Li, G.H., 2008. Comprehensive database on concrete creep and shrinkage. ACI Mater. J. 105, 635–637.
Bažant, Z.P., Prasannan, S., 1988. Solidification theory for aging creep. Cement Concr. Res. 18, 923–932.
Bažant, Z.P., Xiang, Y., 1997. Crack growth and lifetime of concrete under long time loading. J. Eng. Mech. 123, 350–358.
Bažant, Z.P., Hauggaard, A.B., Baweja, S., 1997. Microprestress-solidification theory for concrete creep. I: aging and drying effects. J. Eng. Mech. 123, 1188–1194.
Ben Haha, M., Le Saout, G., Winnefeld, F., Lothenbach, B., 2011. Influence of activator type on hydration kinetics, hydrate assemblage and microstructural development of alkali activated blast-furnace slags. Cement Concr. Res. 41, 301–310.
Bentz, D.P., Peltz, M.A., Winpigler, J., 2009. Early-age properties of cement-based materials . II : influence of water-to-cement ratio. J. Mater. Civ. Eng. 21, 512–518.
Bentz, D.P., Barrett, T., De La Varga, I., Weiss, W.J., 2012. Relating compressive strength to heat release in mortars. Adv. Civ. Eng. Mater. 1.
Bernard, O., Ulm, F.J., Lemarchand, E., 2003. A multiscale micromechanics-hydration model for the early-age elastic properties of cement-based materials. Cement Concr. Res. 33, 1293–1309.
Bijen, J., 1996. Benefits of slag and fly ash. Construct. Build. Mater. 10, 309–314.
Binder, E., Königsberger, M., Díaz Flores, R., Mang, H.A., Hellmich, C., Pichler, B.L.A., 2023. Thermally activated viscoelasticity of cement paste: minute-long creep tests and micromechanical link to molecular properties, Cem. Concr. Res. 163, 107014.
Boltzmann, L., 1878. Theorie der elastischen Nachwirkung [Regarding the theory of creep recovery]. Ann. Phys. 241, 430–432.
Brooks, J.J., 2005. 30-Year creep and shrinkage of concrete. Mag. Concr. Res. 57, 545–556.
Carette, J., Staquet, S., 2016. Monitoring and modelling the early age and hardening behaviour of eco-concrete through continuous non-destructive measurements: Part I. Hydration and apparent activation energy. Cem. Concr. Compos. 73, 10–18.
Caron, R., Patel, R.A., Miron, G.D., Le Galliard, C., Lothenbach, B., Dehn, F., 2023. Microstructure development of slag activated with sodium silicate solution: experimental characterization and thermodynamic modeling. J. Build. Eng. 71, 106398.
Chen, Z., Sorelli, L., Frech-Baronet, J., Sanahuja, J., Vandamme, M., Chen, J., 2017. Duality between creep and relaxation of a cement paste at different levels of relative humidity: characterization by microindentation and analytical modeling. J. Nanomechanics Micromechanics. 7, 1–12.
Dai, X., Aydın, S., Yardımcı, M.Y., Lesage, K., De Schutter, G., 2020. Effects of activator properties and GGBFS/FA ratio on the structural build-up and rheology of AAC. Cement Concr. Res. 138, 106253.
Dai, X., Aydin, S., Yardimci, M.Y., Lesage, K., De Schutter, G., 2022. Early age reaction, rheological properties and pore solution chemistry of NaOH-activated slag mixtures. Cem. Concr. Compos. 133, 104715.

Deir, E., Gebregziabiher, B.S., Peethamparan, S., 2014. Influence of starting material on the early age hydration kinetics, microstructure and composition of binding gel in alkali activated binder systems. Cem. Concr. Compos. 48, 108–117.
Delsaute, B., 2016. New Approach for Monitoring and Modelling of the Creep and Shrinkage Behaviour of Cement Pastes , Mortars and Concretes since Setting Time, p. 362.
Delsaute, B., Staquet, S., 2019. Development of strain-induced stresses in early age concrete composed of recycled gravel or sand. J. Adv. Concr. Technol. 17, 319–334.
Delsaute, B., Staquet, S., Boulay, C., 2012. Monitoring of the creep and the relaxation behaviour of concrete since setting time, part 2 : traction. Strateg. Sustain. Concr. Struct. 10.
Delsaute, B., Boulay, C., Staquet, S., 2016a. Creep testing of concrete since setting time by means of permanent and repeated minute-long loadings. Cem. Concr. Compos. 73, 75–88.
Delsaute, B., Boulay, C., Granja, J., Carette, J., Azenha, M., Dumoulin, C., Karaiskos, G., Deraemaeker, A., Staquet, S., 2016b. Testing concrete E-modulus at very early ages through several techniques: an inter-laboratory comparison. Strain 52, 91–109.
Delsaute, B., Torrenti, J.M., Staquet, S., 2017. Modeling basic creep of concrete since setting time. Cem. Concr. Compos. 83, 239–250.
Diaz, E.I., Allouche, E.N., 2010. Recycling of Fly Ash into Geopolymer Concrete: Creation of a Database. IEEE Green Technol (2010) 0–6.
Feldman, R.F., 1968. A model for hydrated Portland cement paste as deduced from sorption-length change and mechanical properties. Mater. Construcción 1, 509–520.
Gebregziabiher, B.S., Thomas, R., Peethamparan, S., 2015. Very early-age reaction kinetics and microstructural development in alkali-activated slag. Cem. Concr. Compos. 55, 91–102.
Gebregziabiher, B.S., Thomas, R.J., Peethamparan, S., 2016. Temperature and activator effect on early-age reaction kinetics of alkali-activated slag binders. Construct. Build. Mater. 113, 783–793.
Göbel, L., Osburg, A., Pichler, B., 2018a. The mechanical performance of polymer-modified cement pastes at early ages: ultra-short non-aging compression tests and multiscale homogenization. Construct. Build. Mater. 173, 495–507.
Göbel, L., Königsberger, M., Osburg, A., Pichler, B., 2018b. Viscoelastic behavior of polymer-modified cement pastes: insight from downscaling short-term macroscopic creep tests by means of multiscale modeling. Appl. Sci. 8.
Gruskovnjak, A., Lothenbach, B., Holzer, L., Figi, R., Winnefeld, F., 2006. Hydration of alkali-activated slag: comparison with ordinary Portland cement. Adv. Cement Res. 18, 119–128.
Hardjito, D., 2005. Studies on Fly Ash-Based Geopolymer Concrete. Curtin University of Technology.
Hardjito, D., Wallah, S.E., Sumajouw, D.M.J., Rangan, B.V., 2004. On the development of fly ash-based geopolymer concrete. ACI Mater. J. 101, 467–472.
Hu, J., Ge, Z., Wang, K., 2014. Influence of cement fineness and water-to-cement ratio on mortar early-age heat of hydration and set times. Construct. Build. Mater. 50, 657–663.
Hu, Z., Hilaire, A., Wyrzykowski, M., Lura, P., Scrivener, K., 2020. Visco-elastic behavior of blended cement pastes at early ages. Cem. Concr. Compos. 107, 103497.
Hu, Z., Wyrzykowski, M., Lura, P., 2021. Comparison of numerical predictions for early-age creep. 4th Int. RILEM Conf. Microstruct. Relat. Durab. Cem. Compos.729–737.
Huanhai, Z., Xuequan, W., Zhongzi, X., Mingshu, T., 1993. Kinetic study on hydration of alkali-activated slag. Cement Concr. Res. 23, 1253–1258.
Irfan-Ul-Hassan, M., Pichler, B., Reihsner, R., Hellmich, C., 2016. Elastic and creep properties of young cement paste, as determined from hourly repeated minute-long quasi-static tests. Cement Concr. Res. 82, 36–49.
Irfan-ul-Hassan, M., Königsberger, M., Reihsner, R., Hellmich, C., Pichler, B., 2017. How water-aggregate interactions affect concrete creep: multiscale analysis. J. Nanomechanics Micromechanics. 7, 1–16.
Ismail, I., Provis, J.L., Van Deventer, J.S.J., Hamdan, S., 2011. The effect of water content on compressive strength of geopolymer mortars. AES-ATEMA Int. Conf. Ser. - Adv. Trends Eng. Mater. Their Appl. 0, 49–56.
Jones, C.A., Grasley, Z.C., 2011. Short-term creep of cement paste during nanoindentation. Cem. Concr. Compos. 33, 12–18.
Juenger, M.C.G., Winnefeld, F., Provis, J.L., Ideker, J.H., 2011. Advances in alternative cementitious binders. Cement Concr. Res. 41, 1232–1243.
Karte, P., Hlobil, M., Reihsner, R., Dörner, W., Lahayne, O., Eberhardsteiner, J., Pichler, B.L.A., 2015. Unloading-Based Stiffness Characterisation of Cement Pastes during the Second. Third and Fourth Day After Production, Strain.
Königsberger, M., Honório, T., Sanahuja, J., Delsaute, B., Pichler, B.L.A., 2021. Homogenization of nonaging basic creep of cementitious materials: a multiscale modeling benchmark. Construct. Build. Mater. 290.
Krizan, D., Zivanovic, B., 2002. Effects of dosage and modulus of water glass on early hydration of alkali-slag cements. Cement Concr. Res. 32, 1181–1188.
Lacante, M., Delsaute, B., Gambacorta, J., Königsberger, M., Staquet, S., 2022. Development of early age autogenous and thermal strains of alkali-activated slag-fly ash pastes. Front. Built Environ. 8, 1–16.
Lenormand, T., Rozière, E., Loukili, A., Staquet, S., 2015. Incorporation of treated municipal solid waste incineration electrostatic precipitator fly ash as partial replacement of Portland cement: effect on early age behaviour and mechanical properties. Construct. Build. Mater. 96, 256–269.
Li, Z., Zhang, S., Liang, X., Ye, G., 2020. Cracking potential of alkali-activated slag and fly ash concrete subjected to restrained autogenous shrinkage. Cem. Concr. Compos. 114, 103767.
Li, Z., Alfredo Flores Beltran, I., Chen, Y., Šavija, B., Ye, G., 2021. Early-age properties of alkali-activated slag and glass wool paste. Construct. Build. Mater. 291, 123326.
Lothenbach, B., Scrivener, K., Hooton, R.D., 2011. Supplementary cementitious materials. Cement Concr. Res. 41, 1244–1256.
Lura, P., Van Breugel, K., Maruyama, I., 2001. Effect of curing temperature and type of cement on early-age shrinkage of high-performance concrete. Cement Concr. Res. 31, 1867–1872.
Naqi, A., Delsaute, B., Königsberger, M., Staquet, S., 2023. Effect of solution-to-binder ratio and alkalinity on setting and early-age properties of alkali-activated slag-fly ash binders. Materials 16, 1–20.
Neithalath, N., 2008. Quantifying the effects of hydration enhancement and dilution in cement pastes containing coarse glass powder. J. Adv. Concr. Technol. 6, 397–408.
Neville, A.M., 1964. Creep of concrete as a function of its cement paste content. Mag. Concr. Res. 16, 21–30.
Neville, A., 1997. Properties of Concrete, fourth ed. Wiley.
Pane, I., Hansen, W., 2005. Investigation of blended cement hydration by isothermal calorimetry and thermal analysis. Cement Concr. Res. 35, 1155–1164.
Pang, X., 2015. The effect of water-to-cement ratio on the hydration kinetics of Portland cement at different temperatures. 14th Int. Congr. Cem. Chem. 1–12.
Powers, T.C., 1968. The thermodynamics of volume change and creep. Mater. Construcción 1, 487–507.
Prinsse, S., Hordijk, D.A., Ye, G., Lagendijk, P., Luković, M., 2020. Time-dependent material properties and reinforced beams behavior of two alkali-activated types of concrete. Struct. Concr. 21, 642–658.
Provis, J.L., Palomo, A., Shi, C., 2015. Advances in understanding alkali-activated materials. Cement Concr. Res. 78, 110–125.
Reddy, K.C., Subramaniam, K.V.L., 2020. Blast furnace slag hydration in an alkaline medium: influence of sodium content and sodium hydroxide molarity. J. Mater. Civ. Eng. 32, 1–10.
Reiss, E.L., 1961. On the quasi-static theory of viscoelasticity. Arch. Ration. Mech. Anal. 7, 402–411.
Roy, D.M., 1999. Alkali activated cements, opportunities and challenges. Cement Concr. Res. 29, 249–254.
Ruiz, M.F., Muttoni, A., Gambarova, P.G., 2007. Relationship between nonlinear creep and cracking of concrete under uniaxial compression. J. Adv. Concr. Technol. 5, 383–393.
Saludung, A., Azeyanagi, T., Ogawa, Y., Kawai, K., 2021. Effect of silica fume on efflorescence formation and alkali leaching of alkali-activated slag. J. Clean. Prod. 315, 128210.
Schmid, S.J., Zelaya-Lainez, L., Lahayne, O., Peyerl, M., Pichler, B.L.A., 2023. Hourly-Repeated Three-Minutes Creep Testing of a Limestone Calcined Clay Cement Paste (LC3). Springer Nature Switzerland.
Serdar, M., Gabrijel, I., Schlicke, D., Staquet, S., 2020. Advanced Techniques for Testing of Cement-Based Materials.
Shi, C., Day, R., 1995. A calorimetric study of early hydration of alkali-slag cements. Cement Concr. Res. 25, 1333–1346.
Snellings, R., Kazemi-Kamyab, H., Nielsen, P., Van den Abeele, L., 2021. Classification and milling increase fly ash pozzolanic reactivity. Front. Built Environ. 7, 1–13.
Tamtsia, B.T., Beaudoin, J.J., 2000. Basic creep of hardened cement paste. A re-examination of the role of water 30, 1465–1475.
Thomas, R.J., Peethamparan, S., 2015. Alkali-activated concrete: engineering properties and stress-strain behavior. Construct. Build. Mater. 93, 49–56.
Vandamme, M., Ulm, F.J., 2013. Nanoindentation investigation of creep properties of calcium silicate hydrates. Cement Concr. Res. 52, 38–52.
Walter, R., 1968. A hypothesis for the creep of hardened cement paste and the influence of simultaneous shrinkage. In: Proc. Struct. Concr. Its Behav. Under Load, pp. 365–387.
Wang, S.D., Scrivener, K.L., 1995. Hydration products of alkali activated slag cement. Cement Concr. Res. 25, 561–571.
Wang, S.D., Scrivener, K.L., Pratt, P.L., 1994. Factors affecting the strength of alkali-activated slag. Cement Concr. Res. 24, 1033–1043.
Wittmann, F.H., 1973. Interaction of hardened cement paste and water. J. Am. Ceram. Soc. 56, 409–415.
Wyrzykowski, M., Scrivener, K., Lura, P., 2019. Basic creep of cement paste at early age - the role of cement hydration. Cement Concr. Res. 116, 191–201.
Ye, H., 2015. Creep mechanisms of calcium–silicate–hydrate: an overview of recent advances and challenges. Int. J. Concr. Struct. Mater. 9, 453–462.